Surface Plasmon Resonance (SPR) based PCF Sensor Design

by

Jannat Ara Mim **(170021008)**
Tajuddin Ahmed Nahid **(170021014)**
Ahmad Jarif Yeasir **(170021021)**

A Thesis Submitted to the Academic Faculty in Partial Fulfillment of the Requirements for the Degree of

BACHELOR OF SCIENCE IN ELECTRICAL AND ELECTRONIC ENGINEERING

Department of Electrical and Electronic Engineering
Islamic University of Technology (IUT)
Gazipur, Bangladesh

May 2022

Surface Plasmon Resonance (SPR) based PCF Sensor Design

Approved by:

16-5-22

Prof. Dr. Mohammad Rakibul Islam

Supervisor and Professor,
Department of Electrical and Electronic Engineering,
Islamic University of Technology (IUT),
Boardbazar, Gazipur-1704.

Date: ...16-5-22

Table of Contents

List of Tables

List of Figures

List of Abbreviations

PCF ..... Photonic Crystal Fiber
SPR ..... Surface Plasmon Resonance
SPP ..... Surface Plasmon Polariton
SPW ..... Surface Plasmon Wave
FEM ..... Finite Element Method
RI ..... Refractive Index
AS ..... Amplitude Sensitivity
WS ..... Wavelength Sensitivity
RIU ..... Refractive Index Unit
CL ..... Confinement Loss
CVD ..... Chemical Vapor Deposition
TiN ..... Titanium Nitride

TiO_2 ..... Titanium Dioxide
Au ..... Gold
EM ..... Electromagnetic
TIR ..... Total Internal Reflection
FOM ..... Figure of Merit
FWHM ..... Full Width Half Maximum
OFC ..... Optical Fiber Conference
PBF ..... Photonic Bandgap Fiber
LSPR ..... Localized Surface Plasmon Resonance
FDTD ..... Finite Difference Time Domain
PML ..... Perfectly Matched Layer
DPSS ..... Double Peak Shift Sensitivity

List of Symbols

n ..... Refractive Index
λ ..... Wavelength
ε_{Au} ..... Gold Permittivity
t_{PML} ..... PML Thickness
t_a ..... Analyte Thickness
t_g ..... Gold Thickness
t_t ..... Titanium Thickness
p ..... Pitch
d ..... Diameter of air holes
ω_D ..... Plasma Frequency
λ_D ..... Damping Frequency
α ..... Confinement Loss
k_0 ..... Wave Number
$\Gamma_L / 2\pi$ ..... Spectral Width
λ_{min} ..... Minimum wavelength resolution
γ ..... Drude Relaxation Rate
dn/dt ..... Thermo-optical Coefficient (Ethanol)
∂T ..... Temperature Variation
$\partial\lambda_{peak}(T)$ ..... Peak Shift due to Temperature Variation

ACKNOWLEDGEMENT

All praises to the Almighty Allah (SWT). By His mercy, we were able to produce outstanding outcomes for our given thesis. Throughout the duration of writing this thesis, we have received an excessive amount of help and assistance. Professor Dr. Mohammad Rakibul Islam, whose expertise was important in conceiving the study topics and technique, is to be honored first. His perceptive criticism inspired us to grow our knowledge and improve our efforts. We would also like to thank all the faculty members of our Electrical and Electronic Engineering department for their thoughtful advice during our studies. They provided us with the resources we needed to go in the proper path and finish our thesis effectively. When necessary, they offered us critical criticism and valuable suggestions. We would also want to thank our parents for their sage advice, understanding and always being helpful to us.

Jannat 16-5-22

JANNAT ARA MIM
Student ID: 170021008

16/5/22

TAJUDDIN AHMED NAHID
Student ID: 170021014

16-5-22

AHMAD JARIF YEASIR
Student ID: 170021021

ABSTRACT

In recent years, many new designs with great sensitivity have been introduced in the field of SPR based PCF sensors. Designing is challenging since most designs exhibit high sensitivity and high loss or have low sensitivity and low loss. In order to achieve high sensitivity, designs become complex. Our work is focused on the PCF-SPR sensors that are fabricate friendly and have high sensitivity with low loss. Our designs feature circular air holes within the PCF and the outer surface is coated with Au along with a layer of TiO_2. Au work as a plasmonic material and TiO_2 layer increases the adhesivity between gold and fiber. All the analysis of the parameters of the sensors are done by implementing the finite element method (FEM) of COMSOL multiphysics 5.3a. Our first sensor exhibits maximum amplitude sensitivity of 4233 RIU^{-1} whereas maximum confinement loss is 6.22 dB/cm. The same sensor has a sensor resolution of 2.36×10^{-6}. In our 2nd design, first gold is used as plasmonic material for which we get maximum AS of 5336 RIU^{-1} and maximum wavelength sensitivity of 40500nm/RIU for a RI range of 1.32-1.43. Later AZO is replaced by gold which has given more sharp peak and increased the RI range to 1.19-1.42. The FOM for Gold was 744 RIU^{-1} and for AZO 440 RIU^{-1}. This sensor is also used to detect temperature where maximum sensitivity is 1.05 nm/^{o}C with a resolution of 0.095^{o}C. In addition to all these, we introduced a novel detection parameter called 'Double Step Verification' for detecting temperature which takes the help of the change in double peak shift of resonance wavelength to determine the temperature. As a result of all these diverse functionality, our sensor can be concluded as a major developer in the detection of a wide range of analytes in bio and chemical fields as well as a step forward in the field of temperature sensing.

Chapter 1

Introduction

1.1 Background

The benefits of using optical sensors are increasing day by day because of its fascinating properties like small size, real time detection, high sensitivity and precision. The most popular optical sensors are based on Surface plasmon resonance(SPR) for detecting bio molecular substances as well as chemical and temperature. Plasmonic sensors work on the principle of Surface plasmon resonance(SPR) phenomena which occurs at the interface of metal-dielectric under certain special conditions [1]. Total internal reflection (TIR) generates an evanescent field which excites metallic electrons, when a p-polarized electromagnetic wave (EM) hits at the interface. Thus Surface plasmon polaritons (SPPs) are generated due to the collective oscillation of electrons at the metal surface. Then changes take place in the wavelength or angle of the incident wave, as the P-polarized EM wave resonates with the SPPs on the metallic surface. Because of continuous oscillation, EM wave's energy gets transmitted to the SPPs which originate surface plasmon waves (SPWs). These waves are very sensitive to the RI of its surrounding environment. Thus slight change in the RI of the medium can be identified through the shift in resonance angle or wavelength [2]. This phenomenon is used to detect different biological chemicals and biochemistry, for environmental monitoring, food testing, salinity measurement [3-4] as well for detecting temperature [5–7]. Some analytes (such as toluene, polydimethylsiloxane, ethanol, benzene, chloroform) are sensitive to temperature. Thus, their RI changes with the environmental temperature. Whenever there is a fluctuation in the analyte's temperature, resonance wavelength shifts which allows the detection of the temperature. This special feature can be used in many crucial applications such as early detection of the acetone condensation, biomedical and environmental monitoring, brain tumor treatment, industrial production etc. [5,6,8,9].

Current SPR sensors mostly depend on either prism coupling or optical fibers [10]. Kretschmann configuration is widely used for prism coupling in which plasmonic metal is coated on the base of a prism [11]. In this configuration, SPR occurs only when the incident angle of the input wave is greater than the critical angle. However, to bring off this certain angle, various optical and mechanical components are employed which makes it heavy and costly. Thus, it becomes less feasible to fabricate and inadequate for remote sensing [12]. To subdue these limitations, PCF merged with SPR has been introduced. It is better than usual prism and fiber-based SPR sensors because of its various advantages such as single mode operation, birefringence, high nonlinearity and extremely low propagation loss [13]. It can be effectively employed in optical devices and fiber lasers because of its flexible, robust and compact structure design [14]. With the advancement of manufacturing and sensing technology in the field of RI detection, PCF sensors open the door to create landmarks in biological and chemical sensing. However previous works on PCF based sensors exhibit low sensitivity and high propagation loss. Therefore, present research works focus on achieving high sensitivity and low propagation loss by altering the geometrical parameters of the PCF [15] such as air hole diameter, pitch size, number of hole rings in cladding, fiber length and number of lattice arrangement. While designing PCF sensors, selection of plasmonic material should be considered wisely, as it has a significant effect on the sensing performance of the sensor.

1.2 Motivation

Biosensor is a sensor used in food analysis, the study of biomolecules and their interactions, medical diagnostics, environmental field monitoring, and biochemical detection systems. The refractive index and wavelength of incoming light affect the sensitivity of sensors and other intrinsic properties. Sensitivity indicates the amount to which the output varies for varying input quantities. The primary issue with these sensors is the lower wavelength shift, which results in inadequate sensitivity. The issue can be resolved by adjusting the refractive index (RI) of the employed analytes. By optimizing structural characteristics such as wavelength, refractive index (RI), thickness and diameter, a longer wavelength may be achieved. Therefore, we must improve

the structural characteristics to increase sensitivity. In addition, we can utilize a chemically stable metal (Au) with a greater wavelength shift. The precision of detection is dependent on the sharpness of the resonance peak. As much as feasible, we need to create a basic design for fabrication with a high degree of sensitivity. The thesis must emphasize the following: simplest design, chemically stable metals, a broader range of RI, and bigger wavelength shifting for increased sensitivity.

1.3 Purpose of research

Our thesis work focus on finding out SPR based RI sensors which has the following advantages:

- ✓ A practical sensor that can be easily fabricated
- ✓ External sensing so that internal metal coating and injecting analyte into the air holes can be avoided.
- ✓ Offers an ultra-wide range of refractive index(RI) detection
- ✓ Exhibits low confinement loss
- ✓ High Amplitude and wavelength sensitivity along with higher resolution and better sensor linearity.
- ✓ Wide range of applications like detecting temperature, bio-analyte and chemical.

1.4 Thesis outline

This thesis report consists of seven distinct chapters. A brief summary of the chapters is provided in this section.

Chapter 2 describes the background of SPR based PCF sensors and also provides literature review of the existing work on the field of SPR based PCF sensors.

Chapter 3 presents a detailed description on Photonic crystal fiber and about its evolution. The characteristics of PCF fiber and how it is different from traditional optical fiber are also discussed in this chapter. The methods and numerical tools such as confinement loss, effective refractive index that has been used are described here.

Chapter 4 provides a brief explanation of Surface Plasmon resonance and its technology. The working principle of SPR based sensors is discussed as well. The prism configuration, SPP, Evanescent Field, plasmon excitation are also briefed in this chapter.

Chapter 5 contains our proposed Quasi Hexagonal Bi-Clustered SPR RI sensor's design and necessary equation that has been used for investigating various parameters like wavelength sensitivity, resolution, FWHM. The designing parameters like air holes, gold layer thickness are optimized to get best performance of our sensor.

Chapter 6 consists of our work where AZO is used as plasmonic material and exhibits an excellent sensing range of RI which is also examined as temperature sensor. The temperature sensor provides a novel parameter 'Double Step Verification' along with traditional sensing.

Chapter 7 draw the conclusion of our research work including socio-economic influence and future scope of our work.

Chapter 2

Background and Literature Review

2.1 Background

SPRs are more in demand for their fine- tuned calibrating property and a diverse set of usages like diagnostics in medical cases, testing, food safety, bio molecular analyte identification, security, gas detection, maintaining water quality, environmental safety monitoring, disease and drug detection, bio-imaging, biochemical analysis, bio-sensing [16-22]. In the early stages, a metallic layer attached with a prism was proposed by Kretschmann in 1968 [23]. Later on, Liedberg et al. reported a prism coupled geometry theory for gas detection in 1983 [19]. However, prism-based SPR sensors cannot operate without auxiliary (moving) opto mechanical parts, which makes it bulky and complex; hence it is not suitable for remote sensing applications [24]. Researchers came up with the idea of using optical fiber instead of prism to surmount these obstructions, where surface plasmons occur through fiber coupling. Miniaturization of SPR biosensor becomes possible by substituting optic fiber. In 1993, R.C. Jorgenson, for the first time, introduced a SPR sensor ideated on optical fiber, where the gold film enveloped the core of fiber to demonstrate the plasmonic reaction [25]. Afterwards, metalized fiber Bragg gratings, metalized single-mode, metalized tapered fibers, polarization maintenance, multimode waveguides and fiber sensors with lapped D-shaped structure have been explored [26-28]. However, photonic crystal fiber(PCF) has been proved better than regular optical fiber owing to its fascinating properties like, high confinement, single-mode of propagation and controllable birefringence [17-22, 24, 29-30], design flexibility, small size [31], propagation in air and solid core [32]. Thus, PCFs are used extensively nowadays for the detection of unknown chemical analytes. Silver, copper and gold are popular as plasmonic materials [32]. Among these materials, silver has the most conduction electron, providing a very sharp resonance peak. However, silver is chemically unstable; for example, oxidation occurs easily with oxygen contact, which can hamper the performance of a sensor [33]. This issue can be solved using a graphene layer above the silver layer, but it causes difficulty in fabrication, leading to extra manufacturing cost [31]. On the contrary, gold is more acceptable because of its inert nature. It also provides a large resonance wavelength shift, which helps in the

case of easy detection and increases the accuracy of the sensor [34]. Researchers have proposed many designs for SPR sensing using different plasmonic materials and adjusting optical parameters, e.g., pitch, diameters of the air holes, and thickness of different layers. In general, two types of sensing approaches are used; internal and external. For internal sensing, the unknown analyte is kept inside the fiber; more precisely, air holes are filled with dielectric liquid. However, this type of PCF also needs internal metal coating, which causes difficulty in the fabrication [35]. Moreover, injecting fluid in the selected air holes and removing fluid to inject new fluid is time-consuming. For this reason, internal sensing is not practicable [35]. D-shaped sensors can be a solution in this case, where an analyte can be set on a flat surface. The D-shaped sensors have also shown high sensing performance reported in [35-39], but it needs side polishing for flat surfaces, which causes difficulty in fabrication. Therefore, an externally metal coated PCF sensor is the most acceptable solution, where the fiber's outer surface is coated with plasmonic material.

2.2 Literature Review

Different kinds of structures have been designed and investigated by researchers to enhance the sensitivity and reduce the fabrication difficulty such as D-shaped, internal sensing and external sensing approaches. In case of internal sensing, air holes are coated with plasmonic material and an analyte is injected into the air holes. Internal metal coating causes fabrication difficulty increasing the cost of manufacturing and also injecting fluid into selected air holes and removing to inject new analyte makes it difficult to use [40]. Nowadays D-shaped structure has grabbed the attention of the researchers as a metal layer can be easily coated on its flat surface [41]. In 2021, I. Danlard et al. [42] proposed dual-polarized quasi D-shaped PCF for RI and temperature sensing. For RI detection, maximum wavelength sensitivity was 5000nm/RIU and maximum amplitude sensitivity was 266.54 RIU^{-1} with a resolution of 2×10^{-5} RIU and for temperature maximum sensitivity is 3 nm/°C. However, though D-shaped can be easily metal coated compared to internal sensing, it needs precise side polishing for flat surfaces.

Thus, till now externally metal coated sensor is most preferable where the plasmonic material is disposed on the outer surface. A recent anisotropic PCF design proposed by A.K Shakya et al. [43] shows maximum WS of 20000 nm/RIU and maximum AS of 3167 RIU^{-1} with resolution of 5×10^{-6} RIU. In 2022, M.R Islam et al. [44] proposed dual cluster and dual array-based biosensor with

maximum amplitude sensitivity of 3807 RIU^{-1} with resolution of 2.63×10^{-6} RIU and maximum wavelength sensitivity of 80,500 nm/RIU with resolution of 1.24×10^{-6} RIU. In 2021, a SPR based temperature sensor [45] has been proposed with a sensitivity of 1.151 nm/°C from 20 °C to 70 °C where gold is used as plasmonic material.

Our proposed designs exhibit better performance in terms of sensitivity and resolution compared to above mentioned works. Proposed designs are also easy to fabricate and simple in structure and have multiple applications.

Chapter 3

An overview of the Photonic Crystal Fiber & Methodology

3.1 Evolvement of Photonic Crystal Fiber

PCFs have a periodic transverse microstructure. Yeh et al. introduced the concept of photonic crystal fiber for the first time in 1978. They proposed coating the core of a fiber with Bragg grating, which is comparable to 1D photonic crystal. P. Russell created a 2D photonic crystal fiber with an air core in 1992. 1996 saw the first mention of PCF at the Optical Fiber Conference (OFC). Since 1996, PCFs have been used in practice as low-loss waveguides. Initial demonstration required four years of technological research, and since then manufacturing procedures have become increasingly complex. It is now feasible to manufacture the microstructure in air-glass PCF to an accuracy of 10 nm on a scale of 1 um. Now we can regulate crucial features such as birefringence, dispersion, nonlinearity, Photonic band gap width and location. By incorporating novel properties like as low-loss guiding in a hollow core, PCF has a vast array of applications.

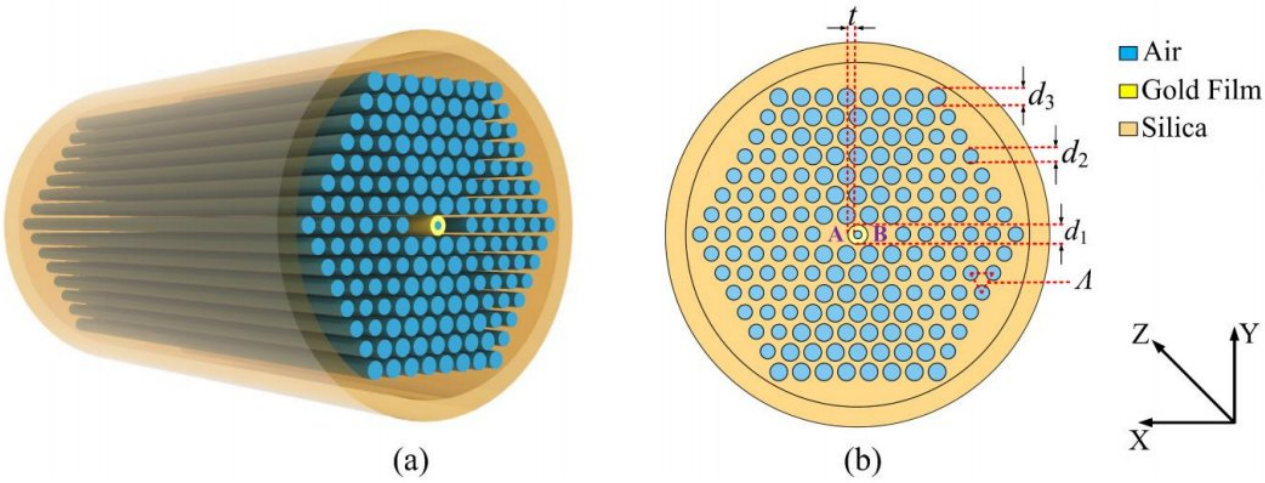

Fig. 3.1: (a) a three-dimensional view of a PCF, (b) cross-sectional view

3.1.1 Brief explanation of PCF

Photonic Crystal Fiber is a type of optical fiber that employs photonic crystals to construct the cladding around the cable's core (PCF). Photonic Crystal is a low-loss dielectric media composed of a periodic grid of small air holes that extends down the whole length of the fiber [46]. PCF traps light in its core and provides photons with a superior wave guide than conventional optical fiber. A solid silica core in PCF is responsible for optical signal guiding. This core is circled by a periodic array of air holes in the cladding. Since the effective cladding index is less than the core refractive index, light signals may be directed along the silica defective core via total internal reflection. The air-holes contribute to the low index cladding, and the core is often made by creating a larger air hole or removing one from the structure's center. PCFs feature a degree of design flexibility, including core radius, number of rings, air hole diameter, and pitch (air hole to hole diameter). As the guiding qualities of optical fibers depend on the refractive index, and the refractive index of PCFs depends on these design freedoms [47], it is possible to modulate these parameters to get guiding properties.

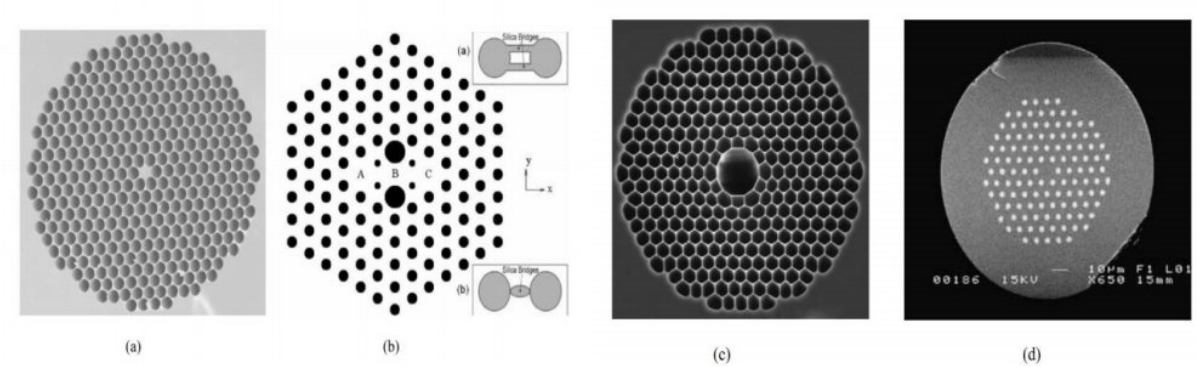

Fig. 3.2: Scanning electron micrographs of different PCF cross-sections (a) a large-mode-area air-silica endlessly single-mode PCF, (b) an air-silica highly birefringent PCF, (c) an air-silica air-core PBF, (d) an all-solid PBF

3.1.2 Difference between Traditional and PCF based Fiber

The core of a standard optical fiber has a greater refractive index than the cladding. Doping a material with a high refractive index into the core area raises its refractive index over that of the silica cladding. Germanium is often used to increase the core's refractive index, whereas fluorine is typically used to decrease it. PCF, on the other hand, is composed of a single substance with extremely minute air holes on a silica base. In traditional fibers, the index contrast between the core and cladding is extremely low, however in PCF, this contrast is quite significant and controllable. This is accomplished by adjusting the differential between two fibers, which results in substantial variations in their optical characteristics [48]. PCF has extremely low or high nonlinearities, broader single mode functioning, great birefringence, and flat dispersion, amongst other characteristics [49].

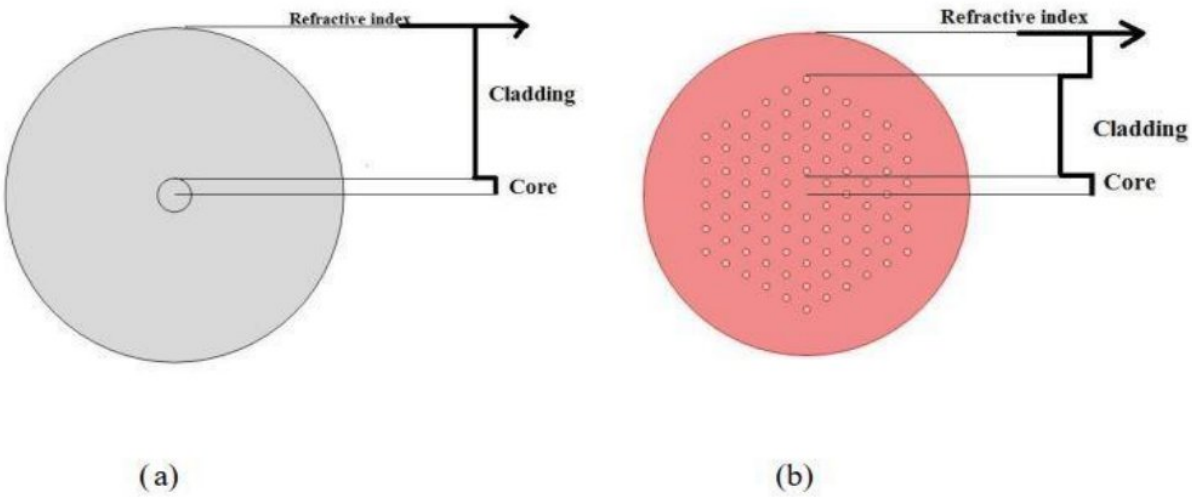

Fig. 3.3: (a) Conventional step-index fiber, (b) Photonic crystal fiber

3.1.3 Light-guiding mechanism of PCF

Photonic crystal fiber is a distinct technological innovation. It often takes the shape of a finite, two-dimensional photonic crystal with a central defect. Several varieties of photonic crystal fibers are utilized in various applications. Photonic crystal fibers are categorized as either solid core or hollow core. Under these two categories, several varieties of photonic crystal fibers exist. Changes can be made to the lattice's symmetry, pitch, and hole size to accommodate the design of a particular fiber type. Solid core fibers have a high-index solid core surrounded by a medium with a lower effective index. The index of the hollow core fibers is less than that of the surrounding medium, and confinement to the center core hole is made feasible by scattering and interference, which combine to generate an evanescent field in the cladding area. [50-51]. Total Internal Reflection (TIR) is the most fundamental and well-known mechanism for light guidance in conventional fibers. [52] The majority of TIR crystal fibers have a solid core surrounded by a coating with a regular periodic pattern of air holes. Photonic crystal fibers (PCFs) are an optical

fibers subtype distinguished by a periodic arrangement of micro capillaries that constitute the cladding around a solid or hollow defect core [53]. Optical characteristics, including modal area, chromatic dispersion, nonlinearity, and birefringence, may be tailored with a great deal of latitude due to the engineering of the PCF shape and the wide variety of accessible materials for its manufacturing. PCFs can display remarkable performance in a wide range of applications, including large-mode-area endlessly single-mode fibers, dispersion rectification, single-polarization and high- birefringence navigation, and nonlinear applications, compared to their conventional counterparts.

3.2 Methodology and Simulation

In this section, all the methods and tools have been discussed which are used for designing and simulating SPR based RI sensors. Without these methods simulation and investigation of our sensor is impossible and these are essential for achieving our goals.

3.2.1 Finite Element Method

The Finite Element Method (FEM) is a numerical technique for treating engineering and mathematical physics challenges. Generally, boundary value problems for partial differential equations are required for the analytical solution of mathematical problems. It formulates the problems and yields an algebraic equation system. The approach provides an estimation of the unknown function across the domain [54]. To tackle the challenge, a complex system is subdivided into smaller, simpler components known as finite elements. The basic equations that represent these finite elements are then included into a larger system that models the full problem. The FEM then approximates a solution by reducing the related error function using a variety of calculus of variations techniques.

3.2.2 Perfectly Matched Layer

A Perfectly Matched Layer (PML) is an artificial absorbing layer for wave equations, often used to truncate computational areas in numerical techniques to model problems with open boundaries, particularly in FDTD and FEM. This permits the PML to substantially absorb outgoing waves from the interior of a computational area without reflecting them back into the interior. PML was originally formulated by Berenger in 1994 to be used with Maxwell equations. Since then, there have been several related reformulations of PML for both Maxwell's equations and for other wave-type equations, such as electrodynamics, the linearized Euler equations, Helmholtz equations, and poroelasticity. The original formulation of Berenger is known as a split-field PML because it divides the electromagnetic fields into two nonphysical fields in the PML area. A newer formulation that has grown more common due to its simplicity and efficacy is known as uniaxial PML or UPML, in which the PML is described as an artificial anisotropic absorbent material [55-57].

3.2.3 Effective Refractive Index

The refractive index may be viewed as the factor by which the speed and wavelength of the radiation are diminished relative to their vacuum values: the speed of light in a medium is $v = c/n$, and similarly, the wavelength in that medium is $\lambda = \lambda 0/n$, where $\lambda 0$ is the wavelength of that light in vacuum. In this study, we optimized resolution and sensitivity by varying the effective refractive index of the layer.

3.2.4 Confinement loss

Confinement losses are the losses caused by the leaky nature of the modes and the imperfect structure of the PCF fiber. Then, depending on the wavelength, number of hole rings, and hole size, modes will be directed with a structure-dependent loss.

This loss is acquired as:

$$\alpha = 8.686 \times k_0 \times \text{Im}\,(n_{eff}) \times 10^4\ (dB/cm) \qquad (3.1)$$

where $k_0 = 2\pi/\lambda$ denotes the free space wave propagation number, is the functioning wavelength, and Im (n_{eff}) is the imaginary part of the effective mode index.

Using Maxwell's equations as an eigenvalue problem with the FEM, the complex RI of the fundamental mode may be solved [58]. This loss varies on core size, pitch and air-hole dimensions, cladding ring count, etc. We must develop an SPR sensor with minimal loss and great sensitivity.

3.2.5 Name of the software

Total 3 software have been used for our thesis work from designing to plotting data. They are:

Comsol Multiphysics version 5.3.a:

Multiphysics software is designed from the bottom up to be multiphysics capable, allowing the user to simply integrate models representing different physics phenomena in any way desired. In some circumstances, this may be accomplished by utilizing the software's built-in functionality, while in others, the user will need to do some additional steps. By setting the sub-domains and boundary conditions with the suitable parameters, we can easily create Photonic Crystal Fiber and solve difficulties for both electric and magnetic fields. Comsol Multiphysics version 5.3.a is used to design the structure.

Microsoft Excel:

It is used to record the acquired data from Comsol software 5.3.a, which are then imported into MATLAB to generate the different curves specified in the preceding section.

MATLAB:

MATLAB is mostly utilized to generate the confinement loss curve, the resolution curve, and the sensitivity curves based on amplitude and wavelength sensitivity.

Chapter 4

Surface Plasmon Resonance and SPR based Sensor

4.1 SPR Theory

Surface Plasmon Resonance (SPR) is the resonant oscillation of conduction electrons at the interface of negative and positive permittivity material induced by incoming light. SPR is the foundation of several conventional techniques for detecting the adsorption of material onto planar metal (usually gold or silver) surfaces or onto the surface of metal nanoparticles. It is the essential idea underlying several color-based biosensor applications, including lab-on-a-chip sensors, and diatom photosynthesis.

4.2 Explanation of SPR

The Surface Plasmon Polariton is a nonradiative electromagnetic surface wave that propagates parallel to the negative permittivity/dielectric material interface. Since the wave is on the threshold between the conductor and the external medium (such as air, water, or vacuum), these oscillations are very sensitive to any change in this boundary, such as the adsorption of molecules to the conducting surface. [59] To characterize the presence and features of Surface Plasmon Polaritons, several models are available (quantum theory, Drude model, etc.). The easiest method to tackle the issue is to view each material as a homogeneous continuum, defined by a frequency-dependent relative permittivity between the external medium and the surface. This amount, which will hereafter be referred to as the material's "dielectric function," is the complex permittivity. In order for the terms that specify the electronic surface plasmon to exist, the real component of the conductor's dielectric constant must be negative and its magnitude must be larger than that of the dielectric. This requirement is satisfied in the infrared-visible wavelength range for air/metal and water/metal interfaces (where the actual dielectric constant of a metal is negative and that of air or water is positive).

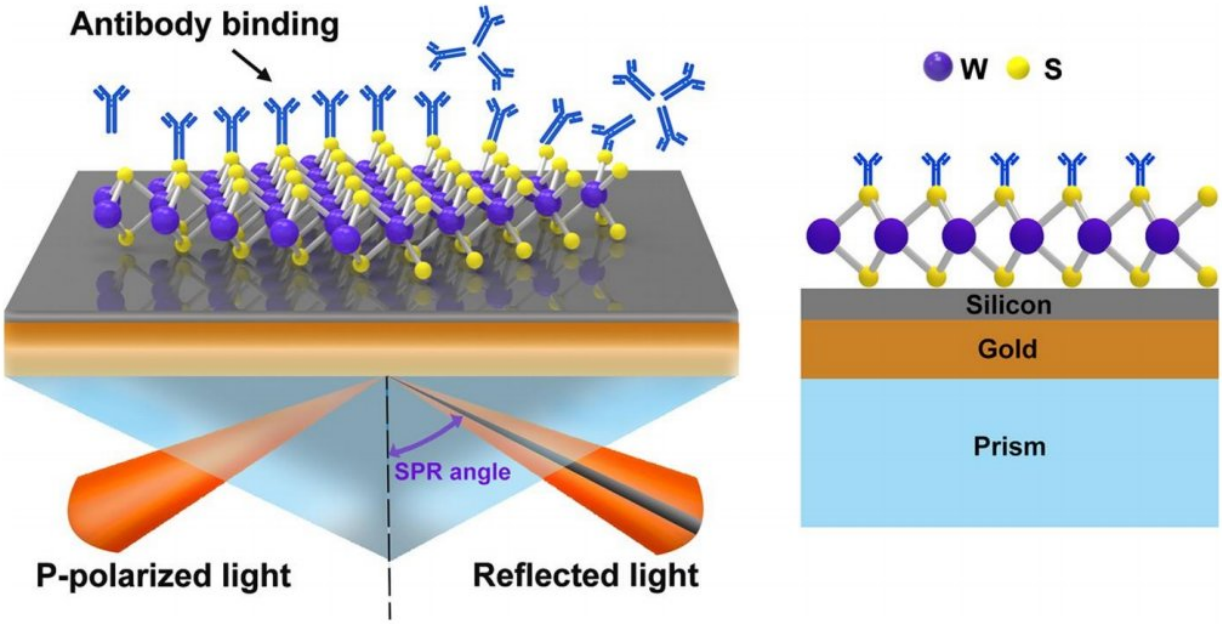

Fig. 4.1: Surface Plasmon Resonance

LSPRs (localized Surface Plasmon Resonances) are light-excited collective electron charge oscillations in metallic nanoparticles. They have an increased nearfield amplitude at the resonance wavelength. This field is extremely concentrated at the nanoparticle and quickly decays away from the nanoparticle/dielectric interface into the dielectric background, however the resonance also enhances the particle's far-field scattering. Enhancement in light intensity is a crucial element of LSPRs, and localization implies that LSPRs have very high spatial resolution (subwavelength), limited only by the size of nanoparticles. Due to the increased field amplitude, phenomena that rely on the amplitude, such as the magneto-optical effect, are likewise amplified by LSPRs. [60]

4.3 Surface Plasmon Polariton

The charge mobility in a surface Plasmon always generates electromagnetic fields outside (as well as inside) the metal. Surface Plasmon Polariton is the whole excitation, comprising both the charge motion and related electromagnetic field. They are a sort of surface wave that are steered along the interface similarly to how light is routed through an optical fiber. Surface Plasmon Polaritons

(SPPs) are electromagnetic waves of infrared or visible frequency that move over a metal-dielectric or metal-air contact. The phrase "surface Plasmon Polariton" indicates that the wave contains both charge mobility in the metal ("surface Plasmon") and electromagnetic waves in the air or dielectric medium ("Polariton"). An SPP will propagate along the contact until its energy is dissipated by absorption in the metal or dispersion in other directions (free space) [61].

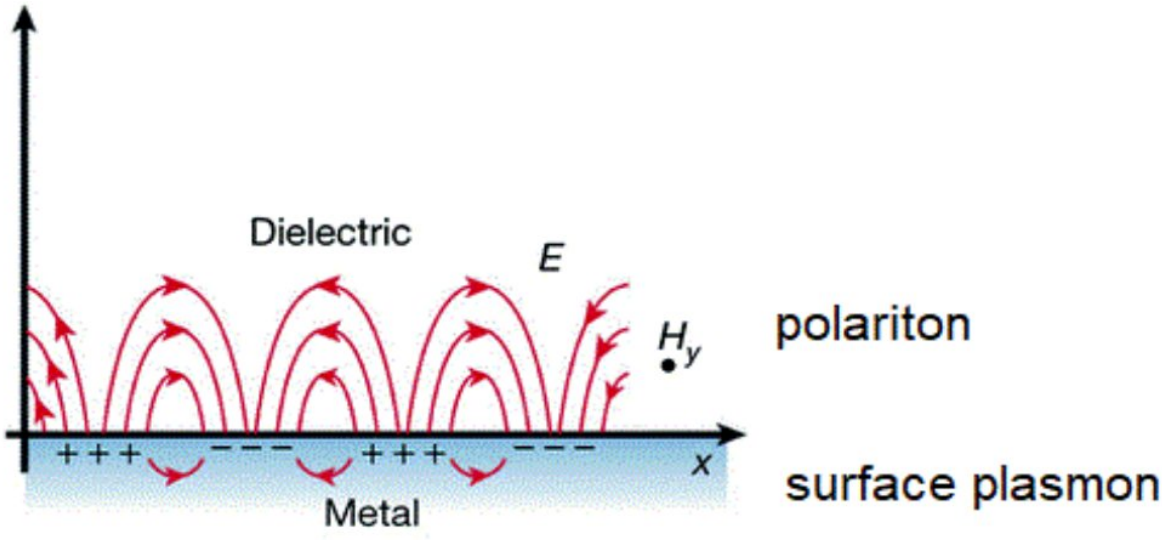

Fig. 4.2: Generation of surface plasmon wave

4.4 Evanescent Field

For light reflecting at angles close to the critical angle, a large percentage of the power extends into the cladding or medium around the core. This phenomenon, known as the evanescent wave, extends just a short distance from the junction, with power decreasing exponentially with distance. Utilizing the evanescent field has enabled real-time investigation of surface-specific recognition events [87]. Fiber optics employ total internal reflection to guide light energy down the fiber, but in reality, a part of the internally reflected wave extends a short distance beyond the core boundary

into the optical cladding. This is the evanescent wave property, which may be used by removing the fiber cladding to enable the evanescent wave to spread beyond the core boundary into substances all around the fiber core. In a system with an absorbing dielectric medium, the strong evanescent electric field increases the medium's absorption.

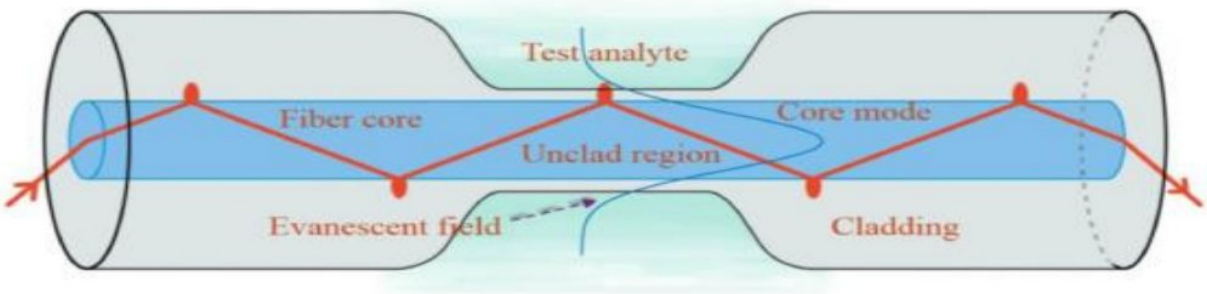

Fig. 4.3: Evanescent field generated in optical fiber

4.5 Plasmon Excitation by Light

Electron bombardment or incident light beam may be used to activate surface plasmons in a resonant fashion (visible and infrared are typical). The entering beam must have the same momentum as the plasmon [62]. In the case of p-polarized light (polarization happens parallel to the plane of incidence), this is accomplished by passing the light through a block of glass to raise the wavenumber (and momentum) and achieve resonance at a particular wavelength and angle. S-polarized light (polarization perpendicular to the plane of incidence) cannot trigger electronic surface plasmons. The next section discusses prism coupling, one of the earliest SPR configurations to be investigated.

4.6 Prism Configuration

When utilizing light to stimulate SP waves, there are two well-known arrangements. In the Otto configuration, light illuminates the wall of a glass block, often a prism, and is completely internally reflected. A thin metal sheet (such as gold) is positioned near enough to the prism wall for an evanescent field to interact with the plasma waves on the surface and thereby excite the plasmons.

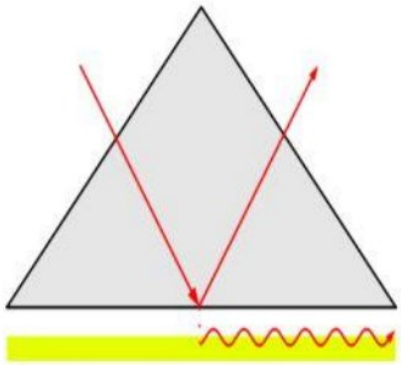

Fig. 4.4: Otto configuration setup

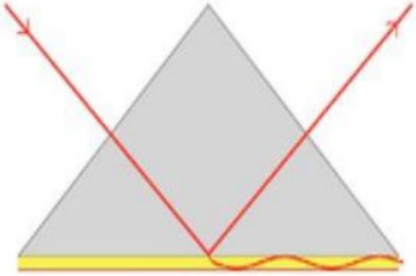

Fig. 4.5: Kretschmann configuration setup

In the Kretschmann setup, the metal film is evaporated onto the glass block. The light once again lights the specimen, and an evanescent wave permeates the metal coating. The plasmons are stimulated on the film's outside surface. This design is used in the majority of practical applications.

4.7 Excitation of SPR in an Optical Fiber

It has been attempted to excite SPR in optical fiber to develop a more compact and dependable sensor with distant sensing capabilities. Excitation of SPR in optical fibers is comparable to SPR excitation in prism arrangement. At the cladding-core and cladding-exterior medium interfaces, modes of light propagating in the fiber core and cladding undergo complete internal reflection.

Different modes impact the cladding-core and cladding-exterior medium interactions from a variety of angles. Numerous successful efforts to implement SPR sensors in optical fibers have resulted from the similarity between light propagation in optical fibers through total internal reflection and prism arrangement. Recent advances have been achieved in SPR, localized SPR, and photonic crystal fiber technologies, and the scientific community is becoming more interested in novel forms of optical fiber SPR-based sensors.

The majority of suggested optical fiber SPR sensors based on metallic nanostructure technologies lack a solid theoretical foundation. In general, published experimental data were used to develop solutions for optical fiber SPR sensors. Complications that arise during the production of sensors may result in alterations to the SPR phase matching condition, a possible widening of SPR, and a consequent reduction in sensitivity. Current study indicates that significant progress has been made in this subject. However, further effort is needed to create new ways and enhance the performance of the suggested sensors so that they are more reliable and simplified.

Chapter 5

Modeling of a Quasi Hexagonal Bi-Clustered SPR Refractive Index Sensor with High Amplitude Sensitivity

5.1 Introduction

This chapter presents an investigation on the performance of the sensitivity of a PCF Refractive Index sensor having unique design specifications. To evaluate fiber guiding properties, Finite Element Method (FEM) is used utilizing monetarily accessible COMSOL Multiphysics version 5.3a. Gold layer has been used as the plasmonic material surrounding the fiber to ensure chemical stability and a single fine coating of TiO_2 supported the improvement of gold attachment with fiber. Two modes- core guided & Surface Plasmon Polariton (SPP) coupled and yielded credible results. Structural air holes' design arrangement inside PCF gives an enhanced sensitivity performance. The proposed PCF-SPR gives extremely reduced confinement losses (CL). Numerous precise investigations on the fiber parameters showed highest amplitude sensitivity (AS) 4233 RIU^{-1} in detecting scope of refractive index (RI) 1.32-1.41. 2.36×10^{-6} and 1.18×10^{-5} are achieved as Amplitude resolution and Wavelength resolution respectively. The highest confinement loss found for this sensor is recorded to be 6.22 dB/cm. Our RI sensor can lead to the exact identification of organic chemical and biological analytes for the proposed design specifications providing good sensitivity with significantly reduced confinement loss.

5.2 Design Methodology

The analyte layer thickness is considered 1 µm for the simplification of numerical computations. The accuracy has been enhanced by using finer size of elements for the fabrication purpose. For analytical purposes, y-polarization has been taken into account as it showed better metal-dielectric coupling in SPP mode. As depicted in Fig. 5.1 (a), a schematic of quasi-hexagonal lattice structure

having circular air holes is shown. The figure represents the geometric arrangement of the PCF RI sensor. COMSOL Multiphysics version 5.3a was used for the design and performance investigation process. The fiber consists of several layers starting with the outermost layer of PML denoted as t_{PML} in the Fig. 5.1 (a) with a thickness of 1.50 µm. This artificial PML layer helps to absorb the radiated energy and at metallic gold surface no EM wave reflection occurs. Underneath the PML, the biochemical analyte used for detection will be passed as denoted by t_a. Analyte layer thickness is selected as 1.00 µm which impacts significantly on the sensitivity. After PML and analyte layers, it has 2 fine sheets of gold (Au) and titanium oxide ($TiO_{2)}$ as t_g and t_t in the figure, respectively. The gold layer having thickness 20 nm is used as plasmonic material for the sensor and has been chosen because of high chemical stability and broader shifts in resonance wavelength. On top of gold, TiO_2 has been used for better bonding of gold with fiber. Fused silica ($SiO_{2)}$ has been used as background material. The cladding region comprises air holes stacked in symmetrical bi-clustered arrangement above & below the core. The design has separation of the 2 clusters at the extreme ends of each cluster, resulting in 2 lateral sideway channels from the core to facilitate the maximum interaction of the Electromagnetic (EM) field with the gold (Au) layer. From the geometric center of fiber, there is no air hole in the horizontal axis. The vertical axis from the core center has a symmetric arrangement of a clustered array of air holes. The core center is kept empty with no air holes in the center to maximize the EM field confinement in core guided mode. Two array stacks of 36 circular holes, 18 on the upper clustered array and 18 on the lower can be drilled following the Stack and Draw method. Among these, 16 air holes are in perfect symmetry having diameter d_1 = 0.9 µm in the upper & lower clusters and two central air holes in both the clusters-above & below. Monitoring a number of findings by differing optical parameters, the ideal values have been found as such: t_{PML} = 1.50 µm, t_a = 1.00 µm, t_g = 20 nm, t_t = 5 nm, p (pitch) = 1.0µm, d_1 = d_2 = 0.9 µm. Fig. 5.1(b) shows the stacked preform structure for the proposed PCF.

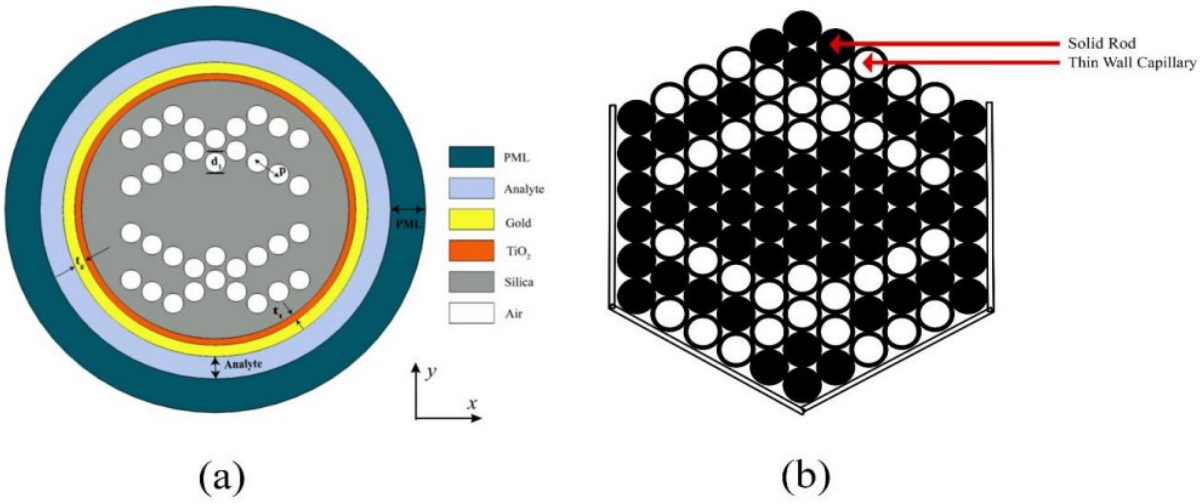

Fig. 5.1 (a) Cross-sectional view of the proposed SPR-based biosensor indicating various parameters; (b) Proposed PCF stacked preform structure.

5.3 Design Factors for Controlling Sensing Performance

The refractive index of TiO_2 can be calculated from the following equation:

$$n_t = \lambda_{resonance} = 187.22 + 276.8932 \times RI_{analyte} + 102.6598 \times RI_{analyte}^{\ 2} \quad (5.1)$$

where λ denotes the wavelength (in Angstroms).

Sellmeir equation is used to obtain the refractive index of fused silica [63] :

$$n^2(\lambda) = 1 + \frac{0.696163\lambda^2}{\lambda^2 - 0.0046791486} + \frac{0.4079426\lambda^2}{\lambda^2 - 0.0135120631} + \frac{0.8974794\lambda^2}{\lambda^2 - 97.934003} \quad (5.2)$$

where n and λ are the refractive index of silica and the wavelength (in µm) respectively.

Gold (Au) chosen as plasmonic material provides the chemical stability shows sharp resonant peak. This helps in accurate detection of the analyte. Drude-Lorentz model has been used to obtain the permittivity of gold [63]:

$$\varepsilon_{Au} = \varepsilon_{\infty} - \frac{{\omega_D}^2}{\omega(\omega + j\gamma_D)} - \frac{\Delta\varepsilon.{\Omega^2}_L}{(\omega^2 - {\Omega^2}_L) + j\Gamma_L\omega} \tag{5.3}$$

where ω_D and λ_D are plasma and damping frequency respectively. Here, ε_{Au} represents the permittivity of gold and $\varepsilon_{\infty} = 5.9673$ is the high frequency permittivity. Other parameters have the numerical values of $\lambda_D /2\pi$ = 15.92 THz, $\omega_D /2\pi$ = 2113.6 THz, and the weighing factor is $\Delta\varepsilon$ = 1.09. Moreover, the oscillator strength and Lorentz spectral width is $\Omega_L/2\pi$ = 650.07 THz and Γ_L $/2\pi$ = 104.86 THz respectively.

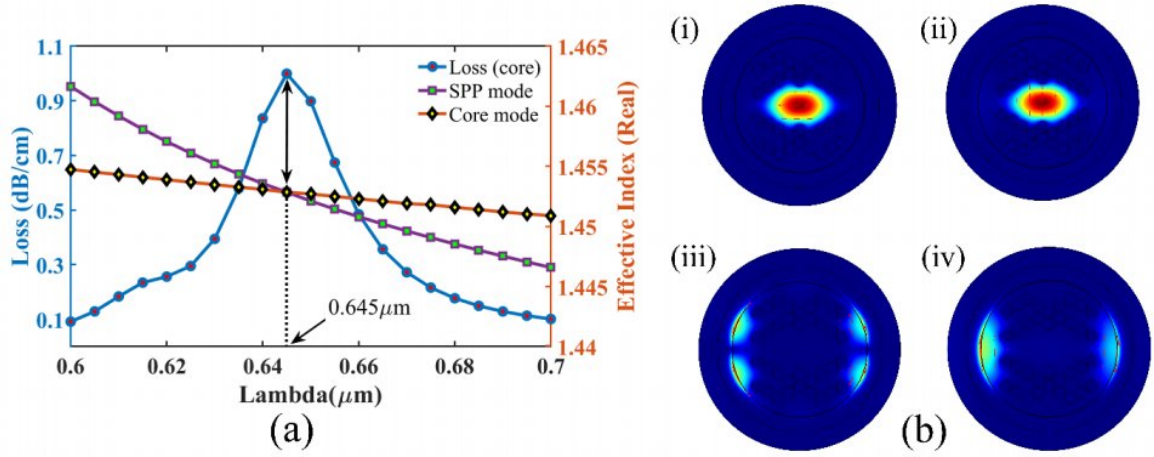

Fig. 5.2: (a) Dispersion relation of core mode and SPP mode at n_a = 1.37; (b) Distribution of optical field at n_a = 1.37 for (i, iii) core mode, SPP mode respectively (x-pol) and (ii, iv) core mode, SPP mode respectively (y-pol).

The dispersion curve of core guided mode (orange line) and SPP mode (violet line) with analyte RI n_a = 1.37 is illustrated in Fig. 5.2 (a). The effective refractive indices (real) of the 2 modes- core and SPP concerning different wavelengths were observed. The real values of the effective refractive indices were plotted against operating wavelengths which generated the curves of dispersion between core mode and SPP mode. Fig. 5.2 (a), solid violet line denotes the real part of n_{eff} of plasmon polariton mode for x-polarization; solid orange line denotes the real part of n_{eff} of plasmon polariton mode for y-polarization. From the figure, we notice that a wavelength of 0.645 µm, n_{eff} of plasmon polariton mode intersects with the n_{eff} of core-guided mode. Thus, phase-matching condition occurs. 0.645µm is obtained as the resonance wavelength for this design. Paramount energy transfer occurs from the core mode to SPP mode at 0.645 µm. Thus, a sharp-edged peak is found in confinement loss. Fig. 5.2 (b) (i, iii) show fundamental core mode, SPP

mode field respectively for x-pol and Fig. 5.2 (b) (ii, iv) fundamental core mode, SPP mode respectively for y-pol. From the figure, we can notice that the core confines maximum of the light for both polarizations. This ensures energetic conjugation between fundamental core mode and SPP mode. However, the y-polarization exhibits a prominent coupling than x-polarization. The coupling strength signifies that there is strong correspondence of generated evanescent field and detection region on the outer side which results in higher accuracy for detection of unknown analytes. For higher loss of the y-polarized mode, stronger conjugation between evanescent field and SPP mode is obtained. The performance of the sensor is improved greatly.

Any PCF-based sensor may use sensitivity to assess its conductivity. In addition to a sensor gram curve being a viable way for calculating the sensitivity of a sensor, we suggest the amplitude and wavelength interrogation method for determining the sensor's sensitivity. However, the wavelength interrogation methodology is spectral-based and uses the change in resonant wavelength to identify the analyte concentration, while the amplitude interrogation technique is intensity-based and uses the difference in modal loss to identify the analyte. However, the employment of a power meter and the needless use of wavelength interpolation renders the amplitude interrogation approach relatively less complex, straightforward, and cost-effective. Using the following formula, the amplitude sensitivity can be obtained [64]:

$$S_A = -\frac{1}{\alpha(\lambda, n_a)} \frac{\partial \alpha(\lambda, n_a)}{\partial n_a} \ (RIU^{-1}) \tag{5.4}$$

where, $\partial\alpha(\lambda, \eta_a)$ denotes variation in confinement loss and $\alpha(\lambda, \eta_a)$ denotes radiation loss.

Sensitivity of wavelength (WS) is another important parameter for performance evaluation. It can be calculated by using following Eq. [63]:

$$S_\lambda(nm / RIU) = \frac{\Delta\lambda peak}{\Delta n_a} \tag{5.5}$$

where, $\Delta\lambda_{peak}$ denotes the shift between resonance peaks and $\Delta\eta_a$ denotes two adjacent analyte RI variation.

Sensor resolution is the smallest of analyte RI changes that the sensor can detect. When $\Delta\lambda_{peak}$ is the wavelength shift between two adjacent loss spectra, and $\Delta\lambda_{min}$ is the minimum shift of operating wavelength for particular RI, sensor resolution is measured by following Eq. [65]:

$$SR = \frac{\partial\lambda_{\min} \times \partial n_a}{\partial\lambda_{peak}} (RIU) \tag{5.6}$$

5.4 Simulation Results

Geometrical parameters of a PCF dictate better sensing performance. Better interaction between the evanescent field and gold surface is determined by thickness of gold sheet t_g, PML t_{PML}, analyte layer t_a, titanium t_t, pitch p, and air hole diameters d_1 & d_2. On checking the best fitted value for different variables, we measured the confinement loss (CL), sensitivity of amplitude and wavelength for different values of a particular variable. The most suitable value for any particular variable was selected depending on the values of CL, AS, and WS. At the beginning, the design specifications were used as such: t_g = 25 nm, t_a = 1.20 µm, t_{PML} = 1.50 µm, t_t = 10 nm, $d_1 = d_2$ = 0.90 µm, p = 1.00 µm and then optimized one by one.

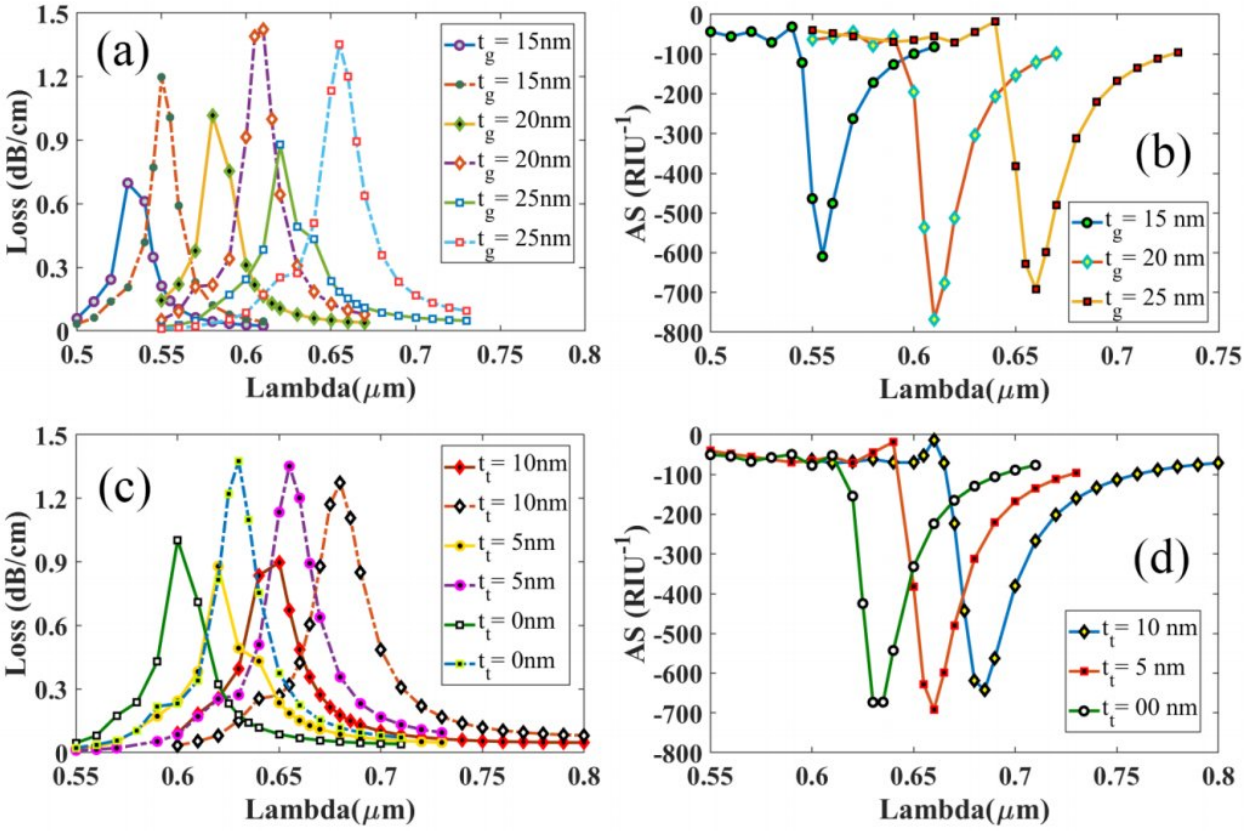

Fig. 5.3: (a) Variation in confinement loss (y-pol) for gold layer thickness-15, 20 and 25 nm at $n_a = 1.37$ (solid lines), and $n_a = 1.38$ (dashed lines); (b) Sensitivity of amplitude (y-pol) varying thickness of gold-15, 20 and 25 nm at $n_a = 1.37$; (c) Variation in confinement loss (y-pol) for TiO_2 layer thickness-10, 5 and 0 nm at $n_a = 1.37$ (solid lines), and $n_a = 1.38$ (dashed lines); and (d) Sensitivity of amplitude (y-pol) varying thickness of TiO_2-10, 5 and 0 nm at $n_a = 1.37$.

The role of gold in the performance of a biosensor is immense. Sensitivity is affected by the thickness of gold film. It was investigated keeping other parameters unchanged. The interaction that occurs in the metal-dielectric layer between the evanescent field and the electrons emitted from the gold layer. This results to the detection of different analytes. Fig. 5.3 (a) and (b) show the influence for varying gold layer thickness on CL and AS of the sensor in y-polarization mode respectively. From the figures, we can see that by increasing the gold thickness, the resonance peak of both CL and AS moves to the right or they have a red shift. Increasing t_g increases confinement loss (CL) but for $t_g = 20$ nm, we have the maximum amplitude sensitivity compared to $t_g = 15$nm and $t_g = 25$ nm. The maximum AS for y-polarization mode obtained are 609.53 RIU

[1], 767.49 RIU^{-1}, 691.75 RIU^{-1} for 15, 20 & 25 nm respectively. Therefore, t_g = 20 nm was chosen as optimum gold layer thickness for further analysis.

After finding the optimum gold thickness, we then analyze thickness of the TiO_2 layer t_t. TiO_2 is used to increase the adhesion of the gold (Au) layer. Variations of loss in confinements changing t_t for n_a = 1.37 and n_a = 1.38 in y-polarized mode are plotted in Fig. 5.3 (c). Fig. 5.3 (d) shows the AS curve at n_a = 1.37. Fig. 5.3 (c) shows that width of TiO_2 layer has a considerable effect on the sensor's sensitivity. Initially, the thickness was taken 10 nm for which we have got CL 0.9 dB/cm and 1.27 dB/cm respectively for RI 1.37, 1.38 and AS was obtained 642.38 RIU^{-1} for RI of 1.37. After decreasing the thickness to 5 nm, the peak has shifted to a lower wavelength and CL is increased as well as AS. Fig. 5.3 (c) and (d) also indicate that without the TiO_2 layer, CL is more remarkable than with the TiO_2 layer, but for t_t = 5 nm the highest AS, which is 691.75 RIU^{-1} is obtained. As mentioned earlier, TiO_2 layer is for the adhesion purpose of gold; without the TiO_2 layer, the Au layer may come off from fiber [38]. Also, as low loss with high sensitivity is more desirable for longer sensor length, 5 nm is taken as the optimized TiO_2 layer thickness.

Fig. 5.4 (a) and (b) depict the pitch variation effect on CL and AS in y-polarization mode, respectively. From Fig. 5.4 (a), it can be observed that the variation of the pitch doesn't have much effect on the shifting of the resonance peak. It has slightly moved to the lower wavelength when pitch has been increased. Depth loss has been increased as pitch is increased by .10 µm resulting in 1.10 µm, illustrated in Fig. 5.4 (a). Obtained AS values in y-polarization are 767.49 RIU^{-1}, 775.57 RIU^{-1}, 750.12 RIU^{-1} respectively for 1 µm, 1.05 µm and 1.10 µm. Though the highest CL is observed for p =1.10 µm, but maximum AS has been obtained for p = 1.05 µm. Thus, for this design, we have chosen 1.05 µm as the optimized pitch layer thickness.

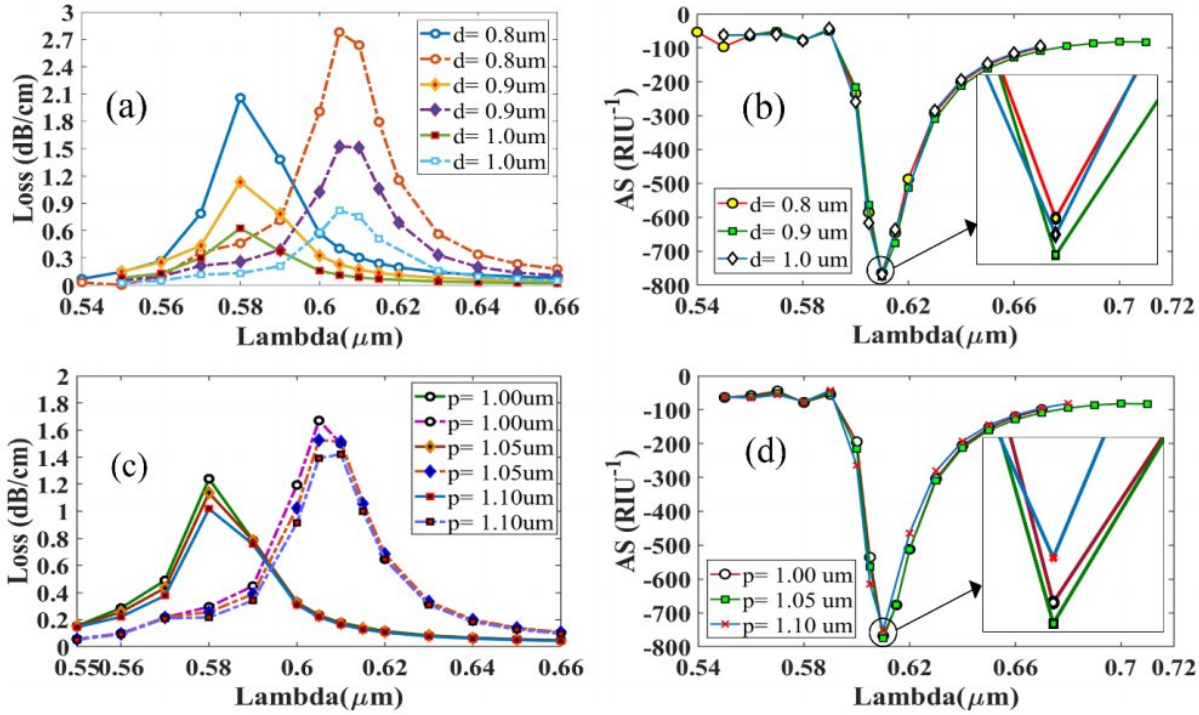

Fig. 5.4: (a) Confinement loss (y-pol) varying diameter-0.8 µm, 0.9 µm, and 1.0 µm at $n_a = 1.37$ (solid lines) and at $n_a = 1.38$ (dashed lines); (b) Sensitivity of amplitude (y-pol) varying diameter-0.8 µm, 0.9 µm, and 1.0 µm at $n_a = 1.37$; (c) Confinement loss (y-pol) varying pitch -1.0, 1.05, and 1.10 µm at $n_a = 1.37$ (solid lines) and $n_a = 1.38$ (dashed lines); (d) Sensitivity of amplitude (y-pol) varying pitch-1.0, 1.05, and 1.10 µm at $n_a = 1.37$.

The air holes' diameter significantly affects the depth loss as seen from Fig. 5.4 (c). The air holes play a vital role in confining light in the core region and guiding the light towards the plasmonic region. But we have observed that it doesn't have any effect on the phase matching wavelength. Therefore, diameter d of air holes doesn't affect the wavelength sensitivity (WS), but certainly it has a vital role in amplitude sensitivity (AS). The air holes' initial diameter was $d_1 = d_2 = 0.90$ µm for which maximum CL was found to be 1.52 dB/cm and highest AS 775.75 RIU^{-1}. After decreasing and increasing the value by 0.1 µm, AS reduced to 764.09 RIU^{-1}, 769.18 RIU^{-1} respectively, showed in Fig. 5.4 (d). Thus we selected the optimized diameter of air holes $d_1 = d_2 = 0.9$ µm. The optimum values of the geometrical parameters have been found for our proposed sensor.

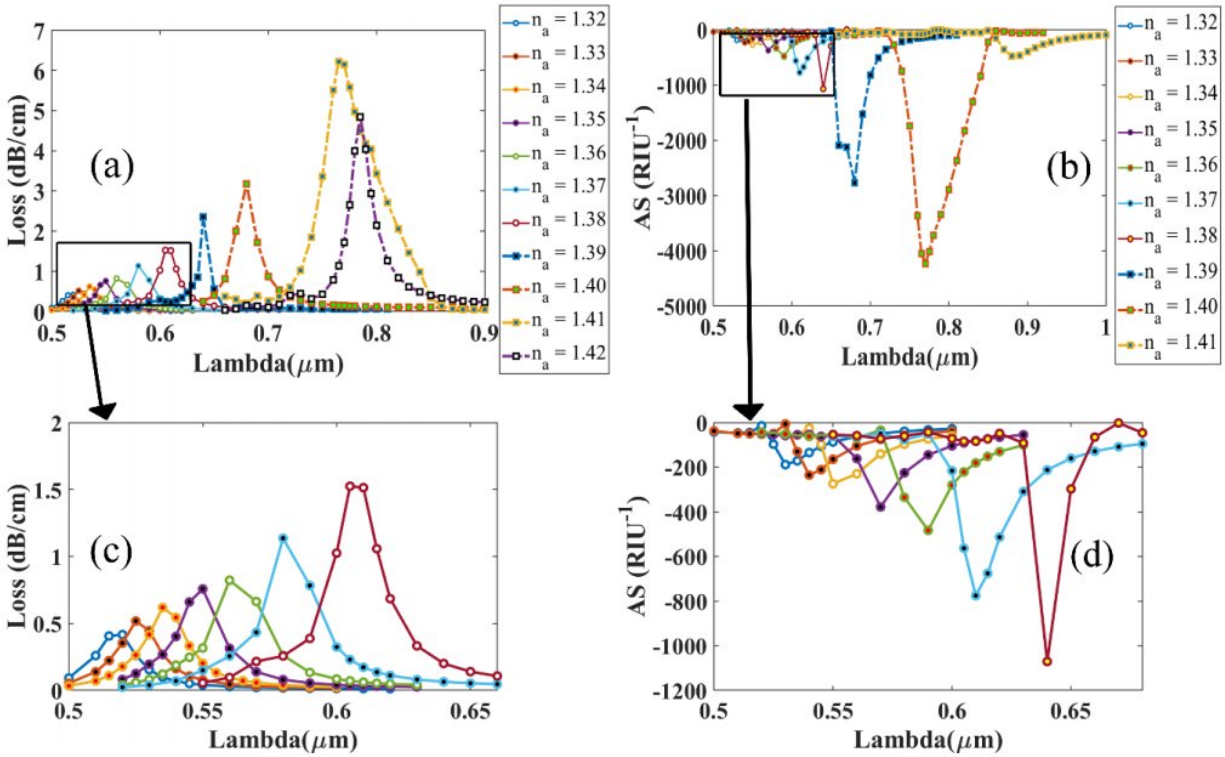

Fig. 5.5: (a) Fundamental core loss variation for increment in RI from 1.32 to 1.42 (y-pol); and (b) Sensitivity of amplitude in RI range 1.33-1.41 (y-pol); (c) Zoomed portion showing fundamental core loss variation and (d) Zoomed portion showing sensitivity of amplitude in marked portion.

We examined how changing refractive index affects the CL and AS. Fig. 5.5 (a) and (b) show effect of changing analyte RI on CL and AS in y-polarization mode respectively. Any slight variation in analyte RI causes the n_{eff} (real) of SPP mode to change which results in blue-shift or red-shift for resonant wavelength [38]. Due to little change of analyte RI, resonant peak wavelength changes rapidly for which WS also changes and depth loss fluctuates from which we obtain AS. From Fig. 5.5 (a), it is observed that due to increase of analyte RI, there is red shift of resonant peak wavelength. CL rises with increase in analyte RI confirming strong interaction between the plasmonic gold material and the EM waves confined in the core [66]. The wide range of analyte RI of 1.32-1.42 can be feasible for application in real-time analysis of biological samples. For 1.32-1.42 analyte RI, the resonance wavelengths are obtained as 520, 525, 535, 550, 560, 580, 605, 640, 680, 765 and 785 nm. The maximum AS obtained was 4232.5 RIU^{-1} for RI of 1.40. In this design, RI range is much wide which provides good accuracy of detection for sensing unknown chemical analytes. From Fig. 5.5 (a), we can see that this sensor design gives sharp peak

loss for RI of 1.32-1.42 but for RI of 1.42 the CL decreases. As a result, Fig. 5.5 (b) illustrates that Amplitude sensitivity for RI=1.41 reduces drastically and the peak becomes almost flat which becomes difficult to detect. So, we did not further increase the analyte RI beyond 1.42.

Besides sensitivity and confinement loss, another parameter, Figure of merit (FOM), helps to understand the comprehensive performance of sensor. The FOM is determined in this paper by following Eq. [67]:

$$FOM = \frac{S_\lambda(nm/RIU)}{FWHM\,(nm)} \tag{5.7}$$

where, S_λ *(nm/RIU)* is Wavelength sensitivity and *FWHM(nm)* denotes full width half-maximum. As FOM is the ratio of WS to FWHM, increase of sensitivity with decrease of FWHM improves the FOM of the sensor.

Table 5.1: Performance analysis of the proposed sensor for different RI

RI	**λ_{peak} (μm)**	**CL (dB/cm)**	**S_A (RIU^{-1})**	**S_λ (RIU^{-1})**	**A_R (RIU)**	**W_R (RIU)**	**FOM (max)**
1.32	0.52	0.41632	188.73	500	5.29×10^{-5}	0.0002	25
1.33	0.525	0.51790	235.77	1000	4.24×10^{-5}	1×10^{-4}	44
1.34	0.535	0.61864	274.51	1500	3.64×10^{-5}	6.67×10^{-5}	66
1.35	0.55	0.75754	378.24	1000	2.64×10^{-5}	1×10^{-4}	47
1.36	0.56	0.82275	482.94	2000	2.07×10^{-5}	5×10^{-5}	94
1.37	0.58	1.13603	775.57	2500	1.29×10^{-5}	4×10^{-5}	120
1.38	0.605	1.52443	1070.6	3500	9.34×10^{-6}	2.85×10^{-5}	162
1.39	0.64	2.34990	2768.1	4000	3.61×10^{-6}	2.50×10^{-5}	280
1.40	0.68	3.17528	4233	8500	2.36×10^{-6}	1.18×10^{-5}	362
1.41	0.765	6.21951	482.69	2000	2.07×10^{-5}	5×10^{-5}	
1.42	0.785	4.84321	-	-	-	-	-

Table 5.1 shows the resonance wavelength, CL, WS, AS, resolution in analyte RI range 1.32-1.41. Highest AS (S_A) of 4233 RIU^{-1}, a maximum amplitude resolution (A_R) of 2.36×10^{-6}, a maximum wavelength resolution (W_R) of 1.18×10^{-5}, highest CL of 6.22 dB/cm is obtained, the FOM of the proposed design for different RI can be observed and it can be also seen that maximum FOM of 362 is obtained at RI = 1.40. R^2 value of 0.9872 is obtained for the quadratic polynomial fitting which indicates better linearity.

5.5 Fabrication Tolerance

Representing the theoretical ideas in the practical scenario is a big challenge. To minimize this hurdle, we have tested whether the variation in the air hole diameters have any effect on the sensitivity. Moreover, we simulated the sensor diameters having values of ±5% and ±10% from the optimized value. From the Fig. 5.6 (a), we can clearly see that the variation in sensing performance is really negligible which indicates to the good fabrication tolerance of the sensor. Stack and Draw method can be implemented to produce the sensor. The commonly used fabrication techniques can be difficult to achieve the precise sensor dimensions. Normally, there occurs a ±2% to ±3% variation from the structural dimension of the design and thus it is necessary to check the fabrication tolerance (FT) analysis [50]. The diameter of the air holes was changed to ±5% and ±10% from the optimized value and Fig. 5.6 (a) showed that the variation in CL was really negligible and didn't affect sensor performance and it is marginal for the change of diameter dimension by ±5% and ±10%.

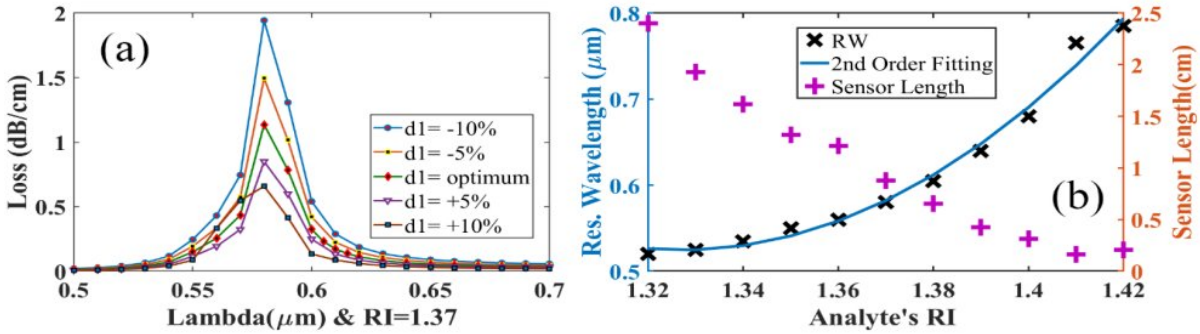

Fig. 5.6: (a) Effects of CL having -10%, -5%, +10% and +5% of d_1; and (b) fiber linearity with optimized geometric parameters of the sensor

Table 5.2: Proposed sensor's comparison with existing sensors in published literature

Ref.	S_A (RIU^{-1})	S_λ (RIU^{-1})	A_R (RIU)	W_R (RIU)	CL (dB/cm)	FOM (max)
[68]	2044	12000	4.89×10^{-6}	8.33×10^{-6}	35	-
[69]	2050	111000	4.88×10^{-6}	9.00×10^{-7}	-	-
[65]	1411	25000	7.09×10^{-6}	4.00×10^{-6}	-	502
[70]	442.11	6000	2.26×10^{-5}	1.66×10^{-5}	449.91	-
[71]	1415	62000	7.07×10^{-6}	1.61×10^{-6}	-	958
[67]	1739.26	9600	5.75×10^{-6}	1.04×10^{-5}	-	-
[66]	1170	34000	7.07×10^{-6}	2.94×10^{-6}	-	310
[72]	1420	11000	7.04×10^{-6}	7.00×10^{-6}	-	407
[73]	318	9000	-	1.11×10^{-5}	700.05	-
Our	4233	8500	2.36×10^{-6}	1.18×10^{-5}	6.22	362

5.6 Discussion

In this chapter, we proposed a gold-coated SPR-PCF sensor with a thin layer of TiO_2 for better adhesion of gold. The sensing approach we are using here is external sensing for y-polarization mode. All the parameters are optimized numerically by Finite Element Method (FEM). After optimizing every parameter, we have got highest amplitude sensitivity 4233 RIU^{-1} and maximum wavelength sensitivity 8500 nm/RIU with very low loss in sensing range of 1.32-1.41. The maximum confinement loss is 6.22 dB/cm, which is very low and thus it is suitable where long sensor length is needed. The resolution (AS) of the sensor is 2.36×10^{-6} which is benefiting to detect analyte precisely. Moreover, the shape of the air holes is circular and diameter is kept same which will lessen the fabrication difficulties. Again the fabrication tolerance of this paper is appreciable. In short, in this design, we are getting high amplitude sensitivity, high sensor resolution and ease of fabrication with a very low confinement loss.

Chapter 6

Design and Analysis of a Highly Sensitive SPR based PCF RI sensor with Double Step Verification for Temperature Sensing

6.1 Introduction

This chapter introduces a comprehensive study of a quad cluster multi-functional Photonic Crystal Fiber (PCF) sensor based on Surface Plasmon Resonance (SPR). As the plasmonic material, both Gold and Aluminum doped Zinc Oxide (AZO) was used and the performance of the respective materials were tested using Finite Element Method (FEM) available in the commercially available COMSOL Multiphysics 5.3a software. Both x and y polarization of the light were considered during the analysis. Following the optimization of multiple parameters, incorporating Gold as the plasmonic material, a maximum Amplitude Sensitivity (AS) of 5269 RIU^{-1} and 5336 RIU^{-1} obtained for x and y polarization respectively. Also, wavelength sensitivity(WS) of 36500 nm/RIU for x polarization and 40500 nm/RIU for y polarization were also obtained. When we included AZO as the plasmonic material, AS of 3593 RIU^{-1} and 3763 RIU^{-1} for x and y polarization respectively were obtained. As well as a WS of 8500 nm/RIU and 9100 nm/RIU for x and y respectively were also determined. We found that the detecting range of RI increased from 1.32-1.43 to 1.19-1.42 after using AZO instead of Au that opens up a new horizon for detection of many other analyte. The highest figure of merit (FOM) for Gold was 744 and 772 RIU^{-1} and for AZO 413 and 440 RIU^{-1} respectively for x and y-pol. As for the sensor resolution, when we used Gold, maximum Amplitude resolution was found as 46.4 $\times 10^{-6}$ RIU for x-pol and 46.3 $\times 10^{-6}$ RIU for y pol. Further, for wavelength resolution, both x and y-pol came as 100×10^{-6} RIU. Compared to Gold, AZO showed a lower Amplitude resolution of 16.1×10^{-6} RIU for x-pol and 15.5 $\times 10^{-6}$ for y-pol but an increased accuracy for Wavelength resolution of 200×10^{-6} RIU for both x and y-pol. Our sensor is also capable of sensing temperature with a maximum sensitivity of 1.05 nm/^{o}C & 1 nm/^{o}C having a resolution of 0.095^{o}C and 0.1^{o}C respectively for x and y-pol. In addition to all these, we introduced a novel detection parameter called 'Double Step Verification' for detecting temperature which takes the help of the change in double peak shift of resonance wavelength to

determine the temperature. As a result of all these diverse functionality, our sensor can be concluded as a major developer in the detection of wide range of analytes in bio and chemical fields as well as a step forward in the field of temperature sensing.

6.2 Proposed Structure and Theoretical Analysis

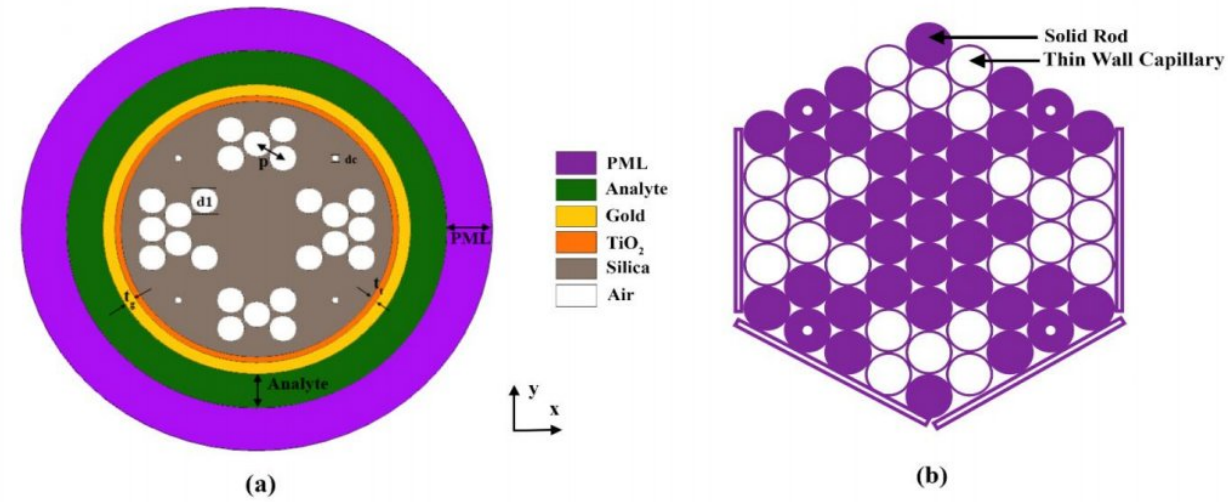

Fig. 6.1: (a) Cross-sectional view of the proposed SPR-based biosensor indicating various parameters; (b) Proposed PCF stacked preform structure.

The cross section of the proposed sensor consists of quad clusters of circular air holes in vertical and horizontal symmetric orientation as illustrated in Fig. 6.1 (a). The upper and lower clusters are made of air holes making a X-shaped pattern all of which has center-to-center distance, pitch p = 1.0 µm constant all over the cladding region. Two types of air holes are involved in the design; 4 corner air holes have comparatively small diameter d_c and the cluster ones are with a regular diameter of d_1. The smallest air holes are placed at four corners of the cladding region to enhance the interaction of the evanescent field with the plasmonic gold layer during SPP mode. Meanwhile,

the air hole clusters on the right and left side are made π-shaped for proper confinement of propagated light in the solid core. Gold and titanium oxide combination has been found to be fruitful for improved gold-fiber adhesion. The fiber is composed of many layers, beginning with the most outer layer of PML, indicated as t_{PML} in Fig. 6.1 (a), which measures 1.50 µm in thickness. This artificial PML layer aids in the absorption of radiated energy, and no EM wave reflection occurs at the metallic gold surface. Behind the PML layer lies the analyte layer t_a, which will be detected by sensor. The core center has been kept solid and free of air holes for maximizing the EM field confinement which occurs for the core guided mode. Solid core mode traps the light right into the middle of fiber producing the core confinement loss. To simplify numerical computation, the thickness of the analyte layer is taken to be 1.20 µm which impacts significantly on the sensitivity. Fused silica (SiO_2) acts as the background material of the sensor and the sensing layer is 20 nm gold coated surface. Gold is preferred as the plasmonic material for higher chemical stability than other metals. Besides, broader shifts of resonance wavelength also serve as a distinct property for gold. The gold coating may be obtained using chemical vapor deposition (CVD) method [28]. In the cladding region, corner placed air holes having smaller diameter (d_c = 0.2 µm) than the rest (d_1 = 0.90 µm), gives rise to leaky nature. Resultantly, the evanescent field excite the electrons in the gold layer and SPR occurs in the metal-dielectric boundary. The design and performance investigation process was carried out using COMSOL Multiphysics version 5.3a. The fabrication process of the PCF can be divided into few stages, including structure design, air hole drilling by Stack & Draw method, preform stacking, preform fusing and final drawing. Fig. 6.1(b) depicts the proposed PCF's layered preform construction. The precision has been increased by fabricating the elements with a finer grain size. For absolute precision of data analysis, both x-polarization & y-polarization were considered. Sensor performance is numerically investigated by using Finite Element Method (FEM). Using a range of different optical parameters, the optimal values have been determined to be as follows: t_{PML} = 1.5 µm, t_a = 1.2 µm, t_g = 20 nm, t_t = 10 nm, p (pitch) = 1.0 µm, d_1 = 0.9 µm and d_c = 0.2 µm.

Sellmeier equation is used for determining the refractive index of the background material SiO_2.

The RI is obtained from the equation [74]:

$$n_{si}^2(\lambda) = 1 + \frac{A_1\lambda^2}{\lambda^2 - B_1} + \frac{A_2\lambda^2}{\lambda^2 - B_2} + \frac{A_3\lambda^2}{\lambda^2 - B_3} \tag{6.1}$$

where n_{si} is the RI of fused silica and λ is the corresponding wavelength measured in μm scale.

The value of Sellmeier coefficients A_1, A_2, A_3, B_1, B_2 and B_3 are taken from [74]. The fluctuation in the RIs of fused silica with temperature is just 1.28×10^{-5} (per degree Celsius). Thus, in normal contexts devoid of significant temperature variations, the influence of temperature is neglected. The plasmonic sensor's detecting performance is strongly sensitive on the plasmonic material. Gold (Au) was chosen as the plasmonic material because it is chemically stable and has prominent resonant peaks. This aids to the analyte's precise detection.

The Drude-Lorentz model is used to determine the dielectric function of Au [74]:

$$\varepsilon_{Au} = \varepsilon_{\infty} - \frac{{\omega_D}^2}{\omega(\omega + j\gamma_D)} - \frac{\Delta\varepsilon.{\Omega^2}_L}{(\omega^2 - {\Omega^2}_L) + j\Gamma_L\omega} \tag{6.2}$$

where ε_{Au} is the permittivity of Au and $\varepsilon_{\infty} = 5.9673$ is the permittivity at a high frequency. Numeric values of other parameters are taken from [30]. As the substitute for gold, AZO was later used as main plasmonic material. The relative permittivity of AZO (2% weight Al) is determined by the following equation for the wavelength range 0.35 μm to 2 μm, as given in [75]:

$$\varepsilon_{AZO} = \varepsilon_b - \frac{{\omega_p}^2}{\omega(\omega + j\gamma_p)} + \frac{f_1{\omega_1}^2}{({\omega_1}^2 - \omega^2 - j\omega\gamma_1)} \tag{6.3}$$

where the polarization response of core electrons (background permittivity) is indicated by ε_b, the plasma frequency is denoted by ω_p, and the Drude relaxation rate is denoted by γ. These parameters have the values: $\varepsilon_b = 3.5402$, $\omega_p = 1.7473$ eV, $\gamma_p = 0.04486$ eV, $\gamma_1 = 0.1017$, $f_1 = 0.5095$ eV, and $\omega_1 = 4.2942$ eV.

Between the silica glass and the Au layer lies a thin TiO_2 layer. Without the TiO_2 coating, the Au adheres poorly and quickly flakes off under little tension. A thin coating of TiO_2 can provide the required adhesive. Additionally, TiO_2 film has a higher RI and behaves as a transition metal, generating an enormous excess of electrons at the surface. A large evanescent wave is generated, which draws the fields from the core into intense interaction with the SPP mode [76].

The refractive index of TiO_2 can be calculated from the following equation [77]:

$$n_t = \sqrt{5.913 + \frac{2.441\times10^7}{\lambda^2 - 0.803\times10^7}} \tag{6.4}$$

where n_t denotes TiO_2's refractive index and is the operational wavelength in the µm scale. It is critical for the plasmonic sensor that the Au and TiO_2 layers are deposited sequentially on the exterior surface of PCF. Numerous coating procedures are available, including thermal evaporation, wheel polishing, and wet-chemistry deposition [78-79]. These methods, however, generate an excessive amount of surface roughness. To address this constraint and film the nano-layer evenly, atomic layer deposition (ALD) and chemical vapor deposition (CVD) technologies are generally deployed [79].

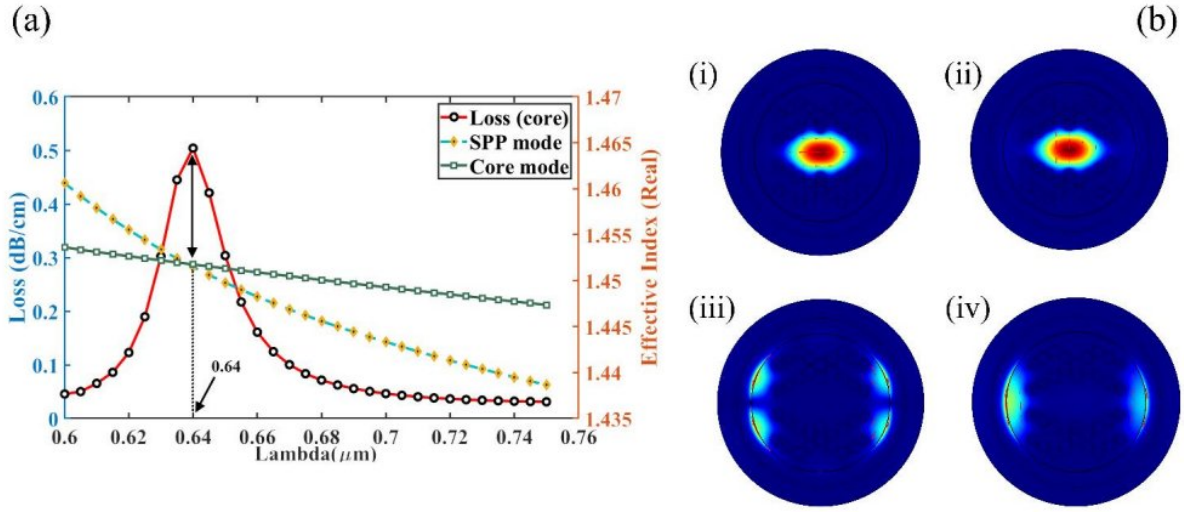

Fig. 6.2: (a) Dispersion relation of core mode and SPP mode at $n_a = 1.37$; (b) Distribution of optical field at $n_a = 1.37$ for **(i, ii)** core mode for x-pol & y-pol respectively and **(iii, iv)** SPP mode x-pol & y-pol respectively.

The effective mode index of the core guided mode steadily decreases when the wavelength of a specific analyte is increased. The dispersion relation in y-polarization mode for analyte RI 1.37 is depicted in Fig. 6.2 (a) presenting curve of core guided mode (green line) and SPP mode (yellow line). The effective refractive indices (real) of the 2 modes- core and SPP concerning different wavelengths were observed. The real values of the effective refractive indices were plotted against

operating wavelengths to get curve between core mode and SPP mode. While both polarized modes exhibit high coupling, the y-polarized mode is significantly stronger than the x- polarized mode. 640 nm for y-polarized mode is the wavelength where the effective index of core-guided and SPP modes meet resulting the peak loss (red line), which is referred to as phase matching. Here maximum portion of energy is transferred from core-guided mode to SPP mode. The proposed sensor guiding properties and the coupling between the core-guided and SPP modes are illustrated in Fig. 6.2 (b). The figures (i) and (ii) illustrate the distribution of the electric field in the core guided mode at analyte RI 1.37 for the x & y-polarized mode, while (iii) and (iv) illustrate the distribution of the electric field in SPP mode for the x & y-polarized mode respectively at same RI 1.37.

6.3 Numerical Analysis and Optimization of Optical Parameters

6.3.1 *Optimization of Au and TiO_2 Thickness*

The sensor's performance is greatly dependent on the fluctuation of the gold layer, as the metal layer generates surface plasmon waves. Due to damping effects, the depth of loss decreases as the gold layer thickness increases [80]. Loss depth & amplitude sensitivity for the difference in gold thickness at analytes RI 1.37 and 1.38 for x polarized mode is depicted in Fig. 6.3 (a) and (b). At analyte RI 1.37(solid lines) & 1.38(dashed lines), the greatest loss depth is 0.557 dB/cm and 0.753 dB/cm respectively, for x polarized mode & a 20 nm thickness. However, at t_g = 25 nm, the lowest loss depths of 0.442 dB/cm and .622 dB/cm for x-polarized mode are detected. Analyzing plots in Fig. 6.3 (a), we observe the CL spectrum exhibits a red-shift response as t_g is increased from 15 to 25 nm. A thin Au layer results in a high coupling between the core guided and SPP modes, whereas a larger Au layer results in a weak coupling and considerable reduction of CL depth. Also in Fig. 6.3 (b), the AS peaks are located at about 608, 820, and 699 RIU^{-1} for t_g = 15, 20, and 25 nm, respectively. The maximum AS is attained at t_g = 20 nm making the optimized Au film thickness 20 nm at n_a = 1.37. Fig. 6.3 (c) and (d) illustrate the loss depth & amplitude sensitivity of the x-polarized mode, respectively, to changes in TiO_2 thickness. A similar pattern has been seen for t_t and t_g variation. With 5, 10, and 15 nm of t_t, the highest CL peaks are about 0.383, 0.557 and .619

dB/cm for n_a = 1.37 and .637, .753, and 0.772 dB/cm for n_a = 1.38. The corresponding AS peaks are seen at about, 820, 751 and 798 RIU^{-1} for analyte RI of n_a = 1.37.

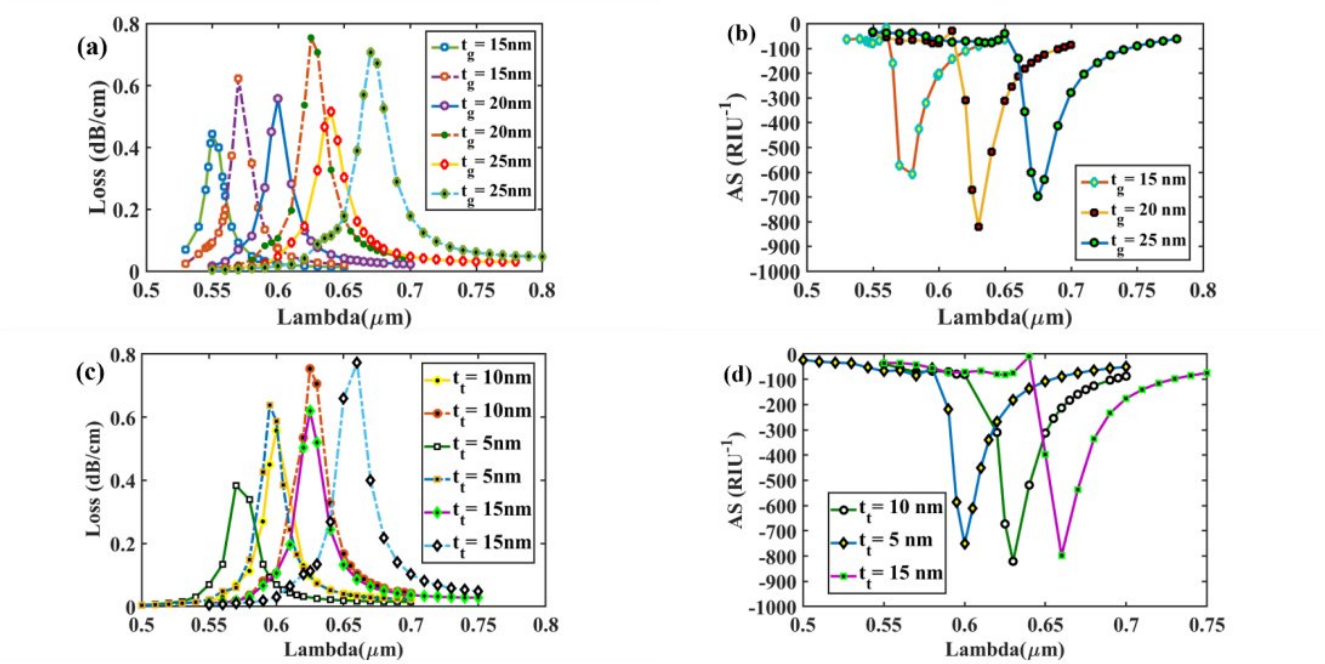

Fig. 6.3: For gold layer thickness-15, 20 and 25 nm, **[x-polarization] (a)** variation in confinement loss at n_a = 1.37 **(solid lines)**, and n_a = 1.38 **(dashed lines)**; **(b)** Sensitivity of amplitude varying at n_a = 1.37; For TiO_2 layer thickness- 10, 5 and 15 nm **(c)** Variation in confinement loss at n_a = 1.37 **(solid lines)**, and n_a = 1.38 **(dashed lines)** and **(d)** Sensitivity of amplitude varying at n_a = 1.37.

Similarly, in Fig. 6.4 (a), (b), (c) and (d) for y-polarized mode, loss depth and amplitude sensitivity for the difference in Au and TiO_2 thickness between analytes RI 1.37 and 1.38 is shown. The AS peaks are located at about 635, 831, and 706 RIU^{-1} for t_g = 15, 20, and 25 nm, respectively. Meanwhile, for TiO_2, the AS peaks- 762, 831, and 815 RIU^{-1} for t_t = 5, 10, and 15 nm, respectively confirming t_g = 20 nm and t_t = 10 nm optimized for both x-polarized and y-polarized mode for this design.

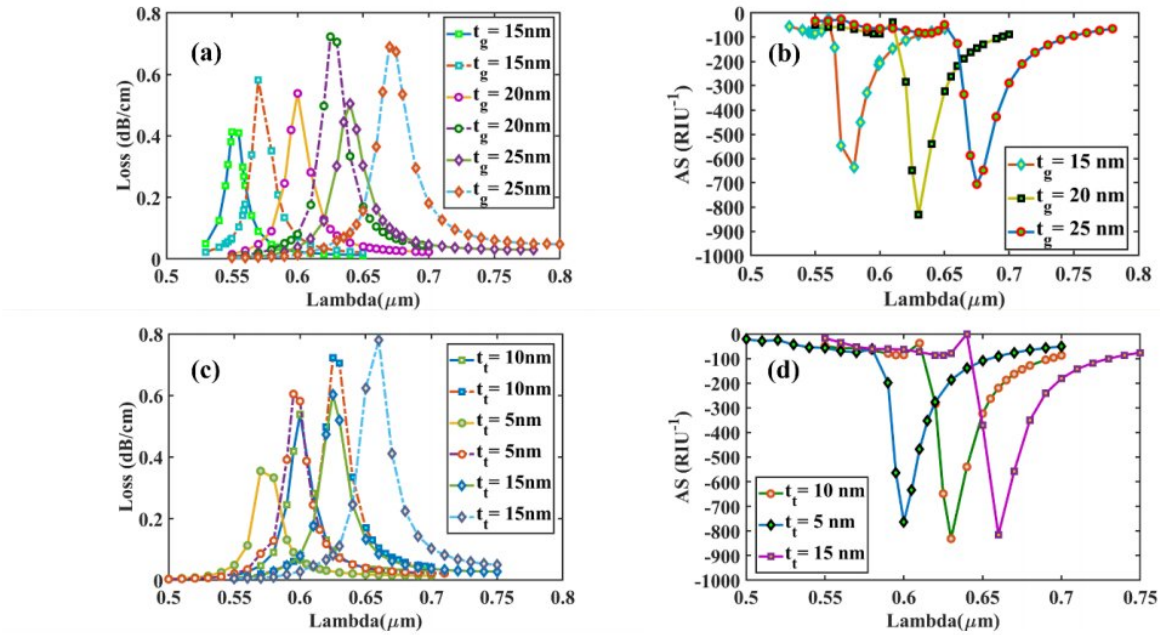

Fig. 6.4: For gold layer thickness-15, 20 and 25 nm, **[y-polarization] (a)** variation in confinement loss at $n_a = 1.37$ **(solid lines)**, and $n_a = 1.38$ **(dashed lines)**; **(b)** Sensitivity of amplitude varying at $n_a = 1.37$; For TiO_2 layer thickness- 10, 5 and 15 nm **(c)** Variation in confinement loss at $n_a = 1.37$ **(solid lines)**, and $n_a = 1.38$ **(dashed lines)** and **(d)** Sensitivity of amplitude varying at $n_a = 1.37$.

6.3.2 Optimization of Air Hole Diameter (d_1) and Pitch (p) size

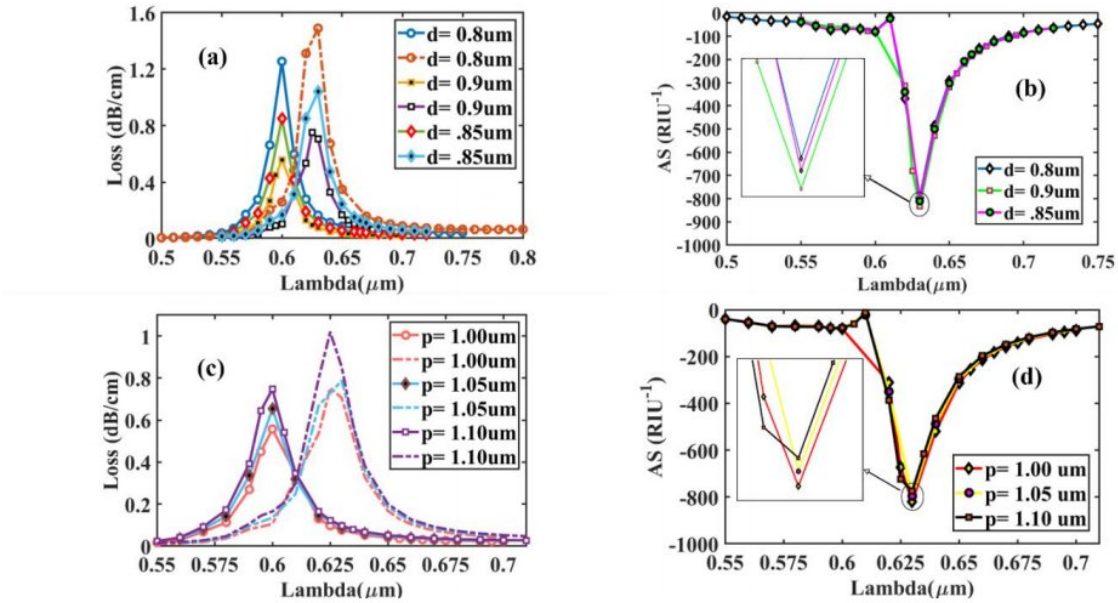

Fig. 6.5: For diameter- 0.8 µm, 0.9 µm, and .85 µm, **[x-polarization] (a)** CL spectrum varying at $n_a = 1.37$ **(solid lines)** and at $n_a = 1.38$ **(dashed lines)**; **(b)** Sensitivity of amplitude at $n_a = 1.37$; For pitch- 1.0, 1.05,

and 1.10 µm **(c)** CL spectrum varying at $n_a = 1.37$ **(solid lines)** and $n_a = 1.38$ **(dashed lines)**; **(d)** Sensitivity of amplitude at $n_a = 1.37$.

Fig. 6.5 (a) illustrate the effect of uniform circular air hole diameter d_1 change on the CL spectra at n_a 1.37 & 1.38 for x-polarized mode. It is obvious to see that as d_1 increases from 0.8 µm to 0.9 µm, the CL curves decrease with values of 1.255, 0.85, and 0.557 dB/cm for d_1 = 0.8, 0.85, and 0.9 µm respectively. However, there was no variation in RW. Additionally, the AS peaks are achieved at approximately 820 (0.9 µm), 810 (0.85 µm), and 795 (0.8 µm) RIU^{-1} for n_a = 1.37, as indicated in Fig. 6.5 (b). Though the CL peaks at d_1 = 0.8 µm, the AS is maximum at d_1 = 0.9 µm. As a result, we identified 0.9 µm as the optimized air hole diameter for this design. Additionally, it is crucial to analyze the pitch (p) variation effect, which has a noticeable effect on sensing performance. To achieve precise sensing performance, we thoroughly calibrated the size, progressively increasing from 1 µm to 1.10 µm. CL spectra variation for n_a at 1.37 & 1.38 x-polarized mode in shown in Fig. 6.5 (c). Pitch modification has almost no influence on the shifting of RW. Obtained AS peak values from Fig. 6.5 (d) are 820 (1.0 µm), 796 (1.05 µm), and 773 (1.10 µm) RIU^{-1} respectively. Maximum AS has been obtained for p = 1.0 µm considered as the optimized pitch layer thickness.

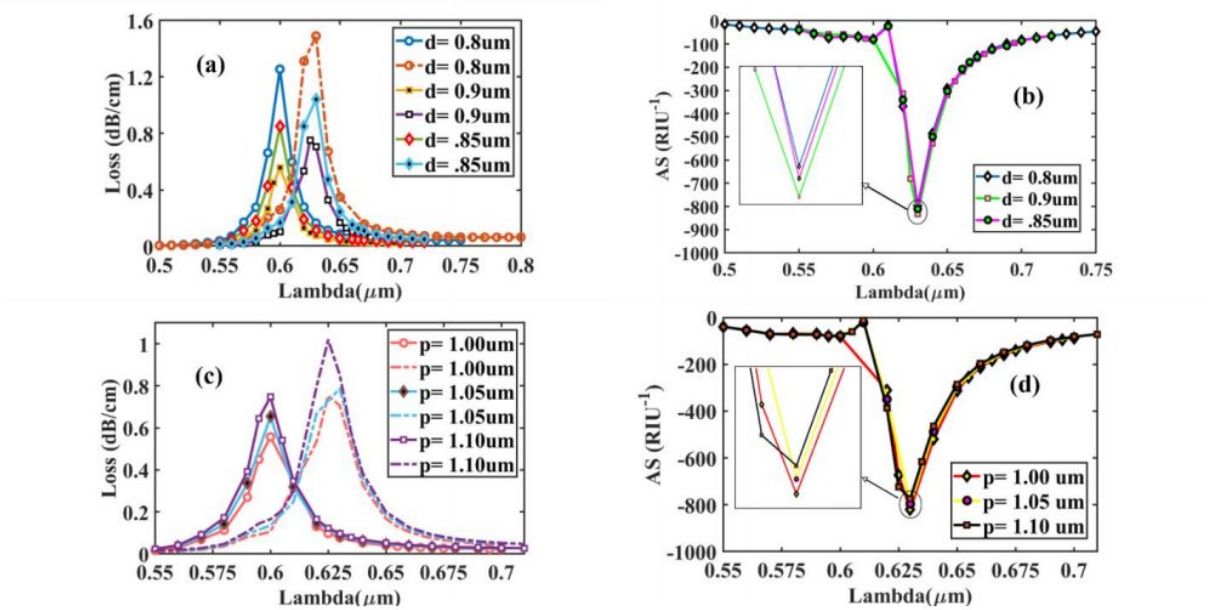

Fig. 6.6: For diameter- 0.8 µm, 0.9 µm, and .85 µm, **[y-polarization] (a)** CL spectrum varying at $n_a = 1.37$ **(solid lines)** and at $n_a = 1.38$ **(dashed lines)**; **(b)** Sensitivity of amplitude at $n_a = 1.37$; For pitch- 1.0, 1.05,

and 1.10 µm **(c)** CL spectrum varying at $n_a = 1.37$ **(solid lines)** and $n_a = 1.38$ **(dashed lines)**; **(d)** Sensitivity of amplitude at $n_a = 1.37$.

Similarly, in Fig. 6.6 (a), (b), (c) and (d) for y-polarized mode, loss depth and AS for the variation of d_1 and p between analytes RI 1.37 and 1.38 is shown. The AS peaks are located at about 831, 822 and 811 RIU^{-1} for $d_1 = 0.9$, 0.85, and 0.8 µm respectively. Meanwhile, for pitch, the AS peaks-831, 809, and 785 RIU^{-1} for p = 1.0, 1.05, and 1.10 µm respectively confirming $d_1 = 0.9$ µm and p = 1.0 µm for this design.

6.3.3 The Effect of Analyte RI variation on Sensing Performance

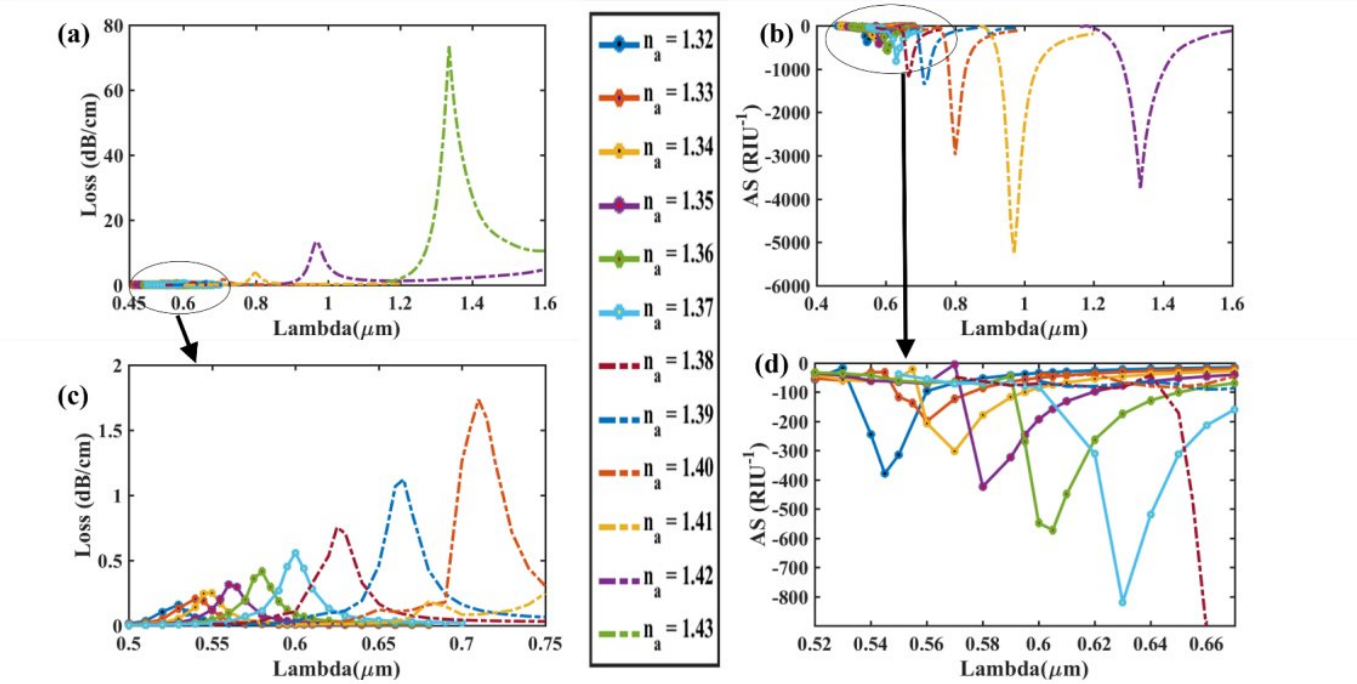

Fig. 6.7: For Au **[x-polarization]** **(a)** Fundamental loss curves for RI of 1.32 to 1.43; **(b)** AS curves in RI range 1.32-1.42 for optimized parameters

Now that the optimal geometrical parameters for our proposed sensor have been determined, we investigate the effect of modifying the refractive index on the CL and AS. Fig. 6.7 (a) and (b) illustrate the effect of varying the RI of the analyte on CL and AS respectively, in the x-polarization mode. Any little fluctuation in the analyte RI produces a change in the n_{eff} (real) of the SPP mode, resulting in a blue or red-shift of the resonant wavelength [81]. As shown in Fig. 6.7 (a), the RW

peak is continuously increasing and relocating to a longer wavelength as analyte RI fluctuates from 1.32 to 1.43. Small changes in n_a may result in a large decrease in the RIs difference between the plasmonic and core guided modes. Thus, the cladding region receives the majority of evanescent light rather than the core region. As a result, light coupling through the metallic surface is enhanced, allowing it to interact efficiently with the dielectric channel. As a result, the CL spectrum gradually increases and causes red-shift. For n_a = 1.32 & 1.33, respectively, the maximum CL spectra were around .159 and .188 dB/cm at RW of 0.53 and 0.54 µm. So, on basis of Eqn. (5.5) in Chapter 5, the WS is about 1000 nm/RIU.

Additionally, the maximum CL spectra found to be around 13.32 and 73.85 dB/cm at RWs of 0.97 and 1.335 µm, respectively, for n_a =1.41 and n_a = 1.42 using Equn. (3.1) in chapter 3. For maximum 365 nm RW shift, maximum WS is found to be 36500 nm/RIU for this sensor in x-polarization. Moreover, the proposed sensor's AS spectra are determined using Eqn. (5.4) in chapter 5, shown in Fig. 6.7 (b). For n_a = 1.32, the minimal AS is about 215 RIU^{-1}. At RW of 0.97 µm, the largest CL peak was seen for n_a = 1.42 while the lowest CL peak was observed for n_a = 1.39. Thus, with n_a = 1.41, the maximum AS of the sensor is calculated to be around 5269 RIU^{-1}. For 1.32-1.43 analyte RI, the resonance wavelengths are obtained as 530, 540, 550, 550, 560, 580, 600, 625, 665, 710, 800, 970, and 1135 nm. Again, in Fig. 6.8 (a) and (b), demonstrate the effect of changing the analyte's RI on CL and AS in the y-polarization mode. The maximum CL spectra found to be around 15.36 and 67.26 dB/cm at RWs of 0.8 and 0.98 µm, respectively, for n_a = 1.41 & 1.42. Highest WS is found to be 40500 nm/RIU for maximum 180 nm RW shift. At n_a = 1.41, maximum AS of the sensor is calculated to be around 5336 RIU^{-1}.

The large range of analyte RI values of 1.32-1.43 makes real-time analysis of biological samples practicable. According to previously published publications [82-84], these sensors operate within the same RI range. The RI range is substantially wider in this design, which results in a high degree of detection accuracy when sensing unknown chemical analytes. FOM is an important parameter for optimizing a sensor's limit of detection. The high FOM value reflects the sensor's superior performance. Thus, using Eqn. (8) in chapter 4, the maximum FOM is approximately 744 & 773 RIU^{-1} for x-polarized & y-polarized mode. Table 6.1 contains the detailed numerical results for Au.

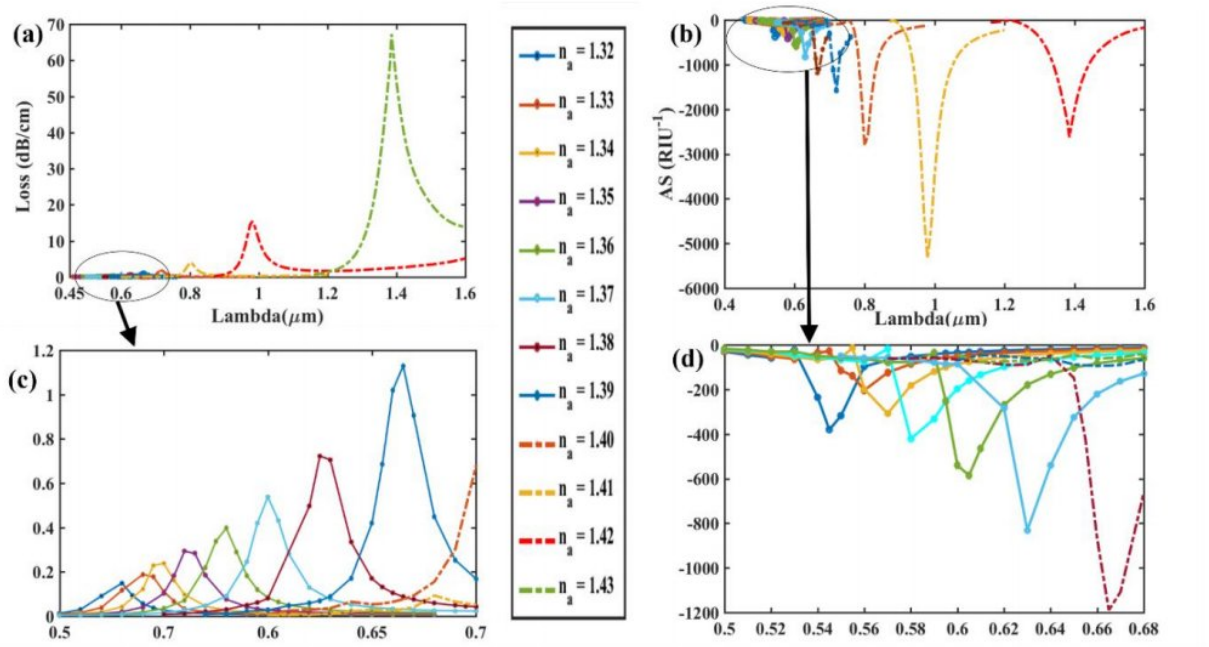

Fig. 6.8: For Au **[y-polarization]** **(a)** Fundamental loss curves for RI of 1.32 to 1.43; **(b)** AS curves in RI range 1.32-1.42 for optimized parameters

6.3.4 The effect of improved RW shift and increased RI range by using AZO as plasmonic material

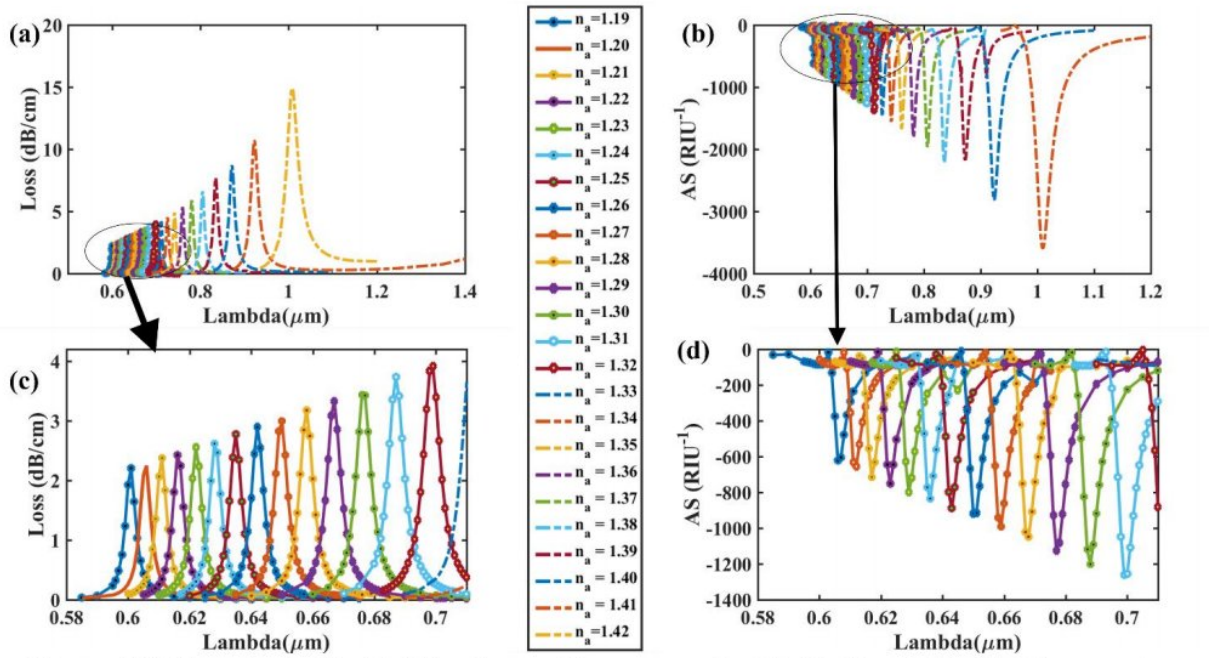

Fig. 6.9: For AZO **[x-polarization]** **(a)** Fundamental loss curves for RI of 1.19 to 1.42; **(b)** AS curves in RI range 1.19-1.41 for optimized parameters

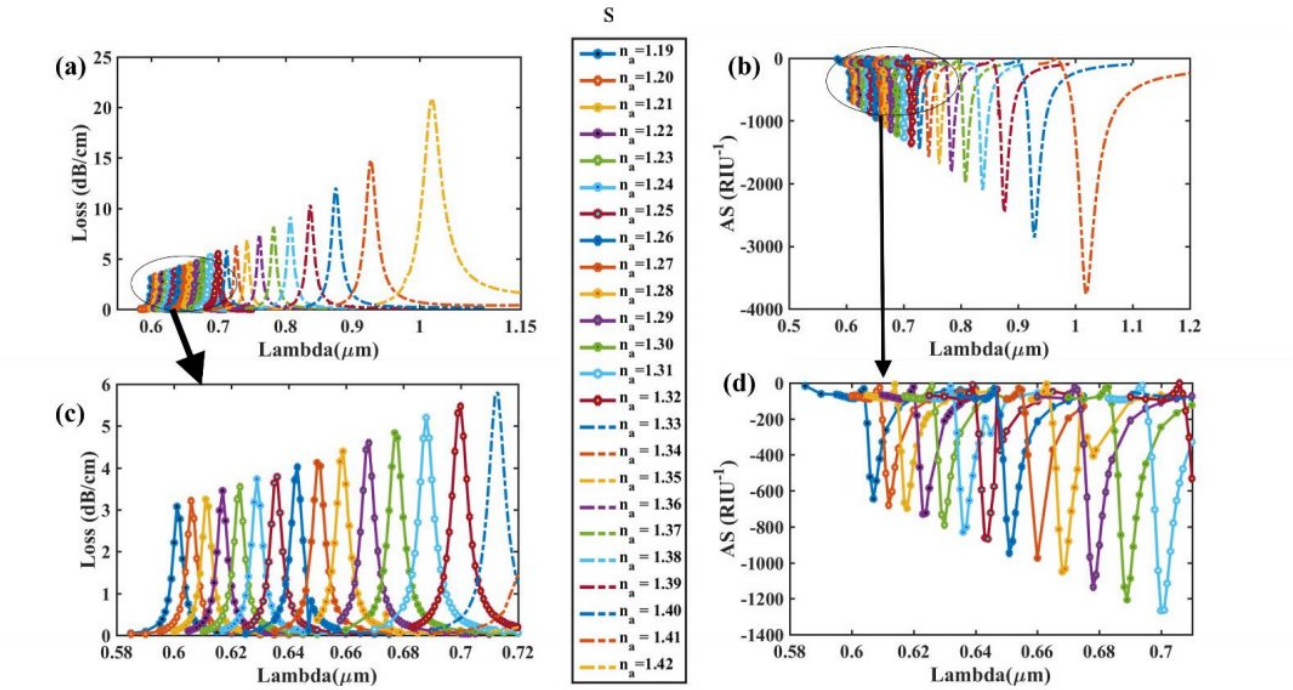

Fig. 6.10: For AZO **[y-polarization]** **(a)** Fundamental loss curves for RI of 1.19 to 1.42; **(b)** AS curves in RI range 1.19-1.41 for optimized parameters

Fig. 6.9 (a) and (b) show the effect of varying the analyte RI on CL and AS respectively, in the x-polarization mode. Highest CL spectra 14.911 dB/cm occurs at n_a = 1.42 at RW of 1.008 µm. Thus, with n_a = 1.41, the maximum AS of the sensor is calculated to be around 3593 RIU^{-1} while the WS is 8500 nm/RIU. To add, most sensitive amplitude resolution & wavelength resolution obtained is 2.78×10^{-6} RIU and 1.18×10^{-5} RIU respectively. The best value of FOM is evaluated as 413. Similarly, for the y-polarization mode, Fig. 6.10 (a) and (b) demonstrate the impact of altering the analyte RI on CL and AS, respectively. At n_a = 1.42 and a RW of 1.018 µm, the highest CL spectra of 20.88 dB/cm occurs. At n_a = 1.41, the sensor's maximum AS is estimated to be around 3763 RIU^{-1}, while the WS is approximately 9100 nm/RIU. Additionally, the maximum amplitude and wavelength resolutions attained are 2.66×10^{-6} RIU and 1.10×10^{-5} RIU, respectively. The peak value of FOM is determined to be 441 for y-polarized mode. Table 6.3 contains the detailed numerical results for AZO & Table 6.4 shows a comparison with existing works with AZO as plasmonic material.

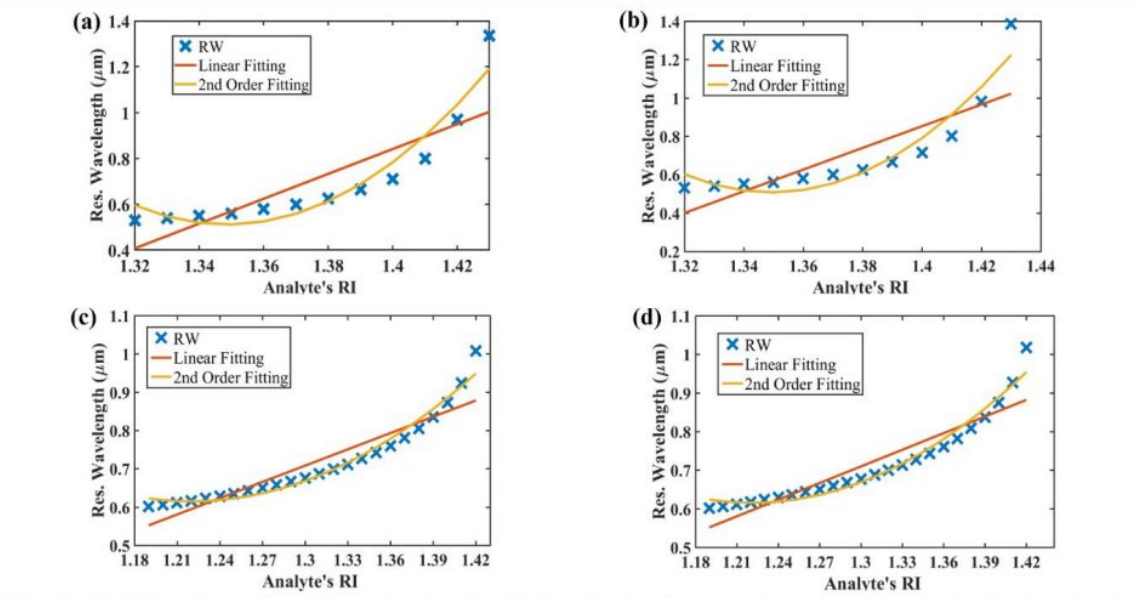

Fig. 6.11: Fiber linearity of **[x-polarization] (a)** optimized parameters & Au; **[y-polarization] (b)** optimized parameters & Au; Linearity **[x-polarization]** (c) optimized parameters & AZO; **[y-polarization] (d)** optimized parameters & AZO.

Fig. 6.11 (a) and (b) illustrate excellent 2nd order fitting curves of the resonance wavelength for Au which indicates the enhanced sensor's high accuracy for determining analyte refractive indices. Value of R^2 is evaluated as 0.9140 and 0.9037 respectively. The fitting curves of 2nd order for AZO is shown in Fig. 6.11 (c) and (d). Table 6.5 depicts the details information about the regression analysis for the sensor where $\lambda_{resonance}$ signifies the resonance wavelength (nm) and $RI_{analyte}$ denotes refractive index of analyte.

Table 6.1

Detailed performance analysis of the sensor for different RI using Au as plasmonic material:

RI	RW(nm)		AS(RIU^{-1})		Amp. Res.(RIU) ($\times 10^{-6}$)		WS(nm/RIU)		Wav. Res.(RIU) ($\times 10^{-6}$)		FWHM		FOM	
	x pol	y pol	x pol	y pol	x pol	y pol	x pol	y pol	x pol	y pol	x pol	y pol	x pol	y pol
1.32	530	530	215.4	215.9	46.4	46.3	1000	1000	100	100	19.57	18.74	51	53
1.33	540	540	255.8	259.8	39.1	38.5	1000	1000	100	100	20.31	19.38	49	52
1.34	550	550	342.0	343.7	29.2	29.1	1000	1000	100	100	18.90	18.24	52	55
1.35	560	560	423.4	420.8	23.6	23.8	2000	2000	50	50	19.35	19.57	103	102
1.36	580	580	548.0	585.1	18.2	17.1	2000	2000	50	50	18.61	25.82	107	77
1.37	600	600	820.7	831.2	12.2	12.0	2500	2500	40	40	19.84	19.73	126	127
1.38	625	625	1178	1187	8.49	8.43	4000	4000	25	25	21.71	22.06	184	181
1.39	665	665	1359	1570	7.36	6.37	4500	5000	22.2	20	23.87	23.66	188	211
1.40	710	715	2982	2882	3.35	3.47	9000	8500	11.1	11.8	30.05	27.25	299	311
1.41	800	800	5269	5336	1.9	1.87	17000	18000	5.88	5.56	34.03	35.23	500	510
1.42	970	980	3775	2624	2.65	3.81	36500	40500	2.74	2.47	49.03	52.40	744	773
1.43	1335	1385	-	-	-	-	-	-	-	-	-	-	-	-

Table 6.2

Comparative study of the performance with existing PCFs as RI sensor:

Refs		Range	AS(RIU^{-1})	Amplitude Resolution(RIU)	WS(nm/RIU)	Wavelength Resolution(RIU)	Figure of Merit (FOM)	DPSS Double Step Verification Sensitivity(nm/ °C)
[82]		1.32-1.41	1170		34000		310	-
[85]		1.413-1.415	1266.67		50000	4.00×10^{-4}	-	-
[75]		1.385–1.40			10000	2.00×10^{-5}	-	-
[86]		1.33-1.42	4358.09	2.29×10^{-6}	21000	4.76×10^{-6}	729	-
[87]		1.35-1.41	4738.9	2.11×10^{-6}	14500	6.90×10^{-6}	387	-
[88]		1.40-1.44	1739.26	5.75×10^{-6}	9600	1.04×10^{-5}	-	-
[89]	x pol	1.33-1.38	371.5	2.69×10^{-5}	4300	2.32×10^{-5}	-	
	y pol		420.4	2.37×10^{-5}	4600	2.17×10^{-5}	-	
This paper	x pol	1.32-1.42	5269	2.65×10^{-6}	36500	2.74×10^{-6}	744	0.35 (1^{st} &2^{nd} peak) 1.90 (2^{nd} & 3^{rd} peak)
	y pol		5336	3.81×10^{-6}	40500	2.47×10^{-6}	773	0.30 (2^{nd} & 3^{rd} peak)

Table 6.3

Detailed performance analysis of the sensor for different RI using AZO as plasmonic material:

RI	RW(nm)		AS(RIU^{-1})		Amp. Res.(RIU) ($\times 10^{-6}$)		WS(nm/RIU)		Wav. Res.(RIU) ($\times 10^{-6}$)		FWHM		FOM	
	x pol	y pol	x pol	y pol	x pol	y pol	x pol	y pol	x pol	y pol	x pol	y pol	x pol	y pol
1.19	601	601	620.6	644.1	16.1	15.5	500	500	200	200	4.15	4.21	120	118
1.20	606	606	656.1	679.6	15.2	14.7	500	500	200	200	4.44	4.24	113	118
1.21	611	611	715.2	698.3	14.0	14.3	500	600	200	167	4.24	4.46	118	134
1.22	616	617	753.1	729.4	13.3	13.7	600	600	167	167	4.54	4.46	132	134
1.23	622	623	797.6	788.9	12.5	12.7	600	600	167	167	4.61	4.64	130	129
1.24	628	629	834.2	830.6	12.0	12.0	700	700	143	143	4.81	4.76	145	147
1.25	635	636	889.7	868.1	11.2	11.5	700	700	143	143	4.94	5.00	142	140
1.26	642	643	919.2	947.4	10.9	10.6	800	700	125	143	5.12	5.13	156	136
1.27	650	650	993	981.8	10.1	10.2	800	900	125	111	5.32	5.42	150	166
1.28	658	659	1020	1050	9.8	9.53	900	900	111	111	5.31	5.56	169	161
1.29	667	668	1125	1136	8.89	8.80	900	900	111	111	5.67	5.86	158	153
1.30	676	677	1203	1206	8.31	8.29	1100	1100	90.9	90.9	6.11	12.51	179	87
1.31	687	688	1263	1265	7.92	7.90	1200	1200	83.3	83.3	6.39	6.37	187	188
1.32	699	700	1363	1362	7.33	7.34	1200	1300	83.3	76.9	6.87	6.80	175	191
1.33	711	713	1444	1465	6.93	6.82	1500	1400	66.7	71.4	7.30	7.32	205	191
1.34	726	727	1550	1575	6.45	6.35	1600	1600	62.5	62.5	7.84	7.74	204	206
1.35	742	743	1676	1687	5.97	5.93	1800	1800	55.6	55.6	8.48	8.38	212	214
1.36	760	761	1805	1813	5.54	5.52	2100	2100	47.6	47.6	9.17	9.23	229	227
1.37	781	782	1966	1990	5.09	5.02	2400	2600	41.7	38.5	10.24	10.28	234	252
1.38	805	808	2217	2105	4.51	4.75	3000	2900	33.3	34.5	11.50	11.49	261	252
1.39	835	837	2175	2456	4.60	4.07	3700	3800	27.0	26.3	13.19	13.39	280	284
1.40	872	875	2819	2851	3.55	3.51	5100	5200	19.6	19.2	15.84	15.85	322	328
1.41	923	927	3593	3763	2.78	2.66	8500	9100	11.8	11.0	20.56	20.65	413	441
1.42	1008	1018	-	-	-	-	-	-	-	-	-	-	-	-

Table 6.4

Comparative study of the performance with existing PCFs using plasmonic material AZO

Refs		Range	AS(RIU^{-1})	Amplitude Resolution(RIU)	WS(nm/RIU)	Wavelength Resolution(RIU)	Figure of Merit (FOM)
[78]			167	-	5000	2.00×10^{-5}	-
[88]		1.31-1.39	3908	-	1700	5.88×10^{-5}	792
[90]		1.27-1.42	4602.67	-	7200	-	1118
This paper	x pol		3593	2.78×10^{-6}	8500	1.18×10^{-5}	413
	y pol	1.19-1.42	3763	2.66×10^{-6}	9100	1.10×10^{-5}	441

Table 6.5

Regression Analysis

Fig. No	Plasmonic material	Curve Fitting Equation	Polynomial Order	R^2 value
6.11 (a)	Au (x pol)	$\lambda_{resonance} = 187.22 + 276.8932 \times RI_{analyte} + 102.6598 \times RI_{analyte}^2$	2nd	0.9140
6.11 (b)	Au (y pol)	$\lambda_{resonance} = 200.66 - 296.6813 \times RI_{analyte} + 109.9401 \times RI_{analyte}^2$	2nd	0.9037
6.11 (c)	AZO (x pol)	$\lambda_{resonance} = 13.034 - 20.3594 \times RI_{analyte} + 8.3438 \times RI_{analyte}^2$	2nd	0.9720
6.11 (d)	AZO (y pol)	$\lambda_{resonance} = 13.351 - 20.8624 \times RI_{analyte} + 8.5437 \times RI_{analyte}^2$	2nd	0.9692

6.3.5 Temperature Sensing

SPR based PCF sensors are becoming more popular in the field of temperature sensing due to high dependence of effective refractive index and confinement loss on temperature [91]. Thus along with analyte sensing our sensor can be used as temperature sensor when temperature sensitive material is used as analyte. In our proposed design we used ethanol as analyte and Aluminum zinc oxide(AZO) as plasmonic material as it has given more sharp peak than gold(Au) according to our numerical investigation. Resonance wavelength shifts significantly as refractive index of ethanol varies with variation in temperature which is the basis of the temperature sensing. The equation used to detect ethanol's RI with temperature variation is [92]:

$$n_1 = n_0 + \frac{dn}{dT}(T_1 - T_0) \tag{6.5}$$

Here, n_0 and n_1 represent refractive indices at temperatures T_0 and T_1, respectively, and dn/dT= -3.117×10^{-4} $^oC^{-1}$ is the thermo-optical coefficient of ethanol. Ethanol's RI is n_0 = 1.361 at temperature T_0= 20 ◦C.

Temperature sensitivity is usually determined by using equation [93]:

$$S_T = \frac{\partial \lambda_{peak}(T)}{\partial T}(nm/°C) \tag{6.6}$$

where S_T , ∂T , $\partial\lambda_{peak}(T)$ mean temperature sensitivity, temperature variation & peak shift due to temperature variation respectively.

Ethanol manifests a boiling point and a melting point of 78.37°C, -114.1°C, respectively. In liquid state of ethanol, its RI varies from 1.343 to 1.403 for temperature variations. Thus, the RI of liquid ethanol range for any temperature aligned with our sensor's detection range. Therefore, our proposed sensor can detect minimum change in environmental temperature.

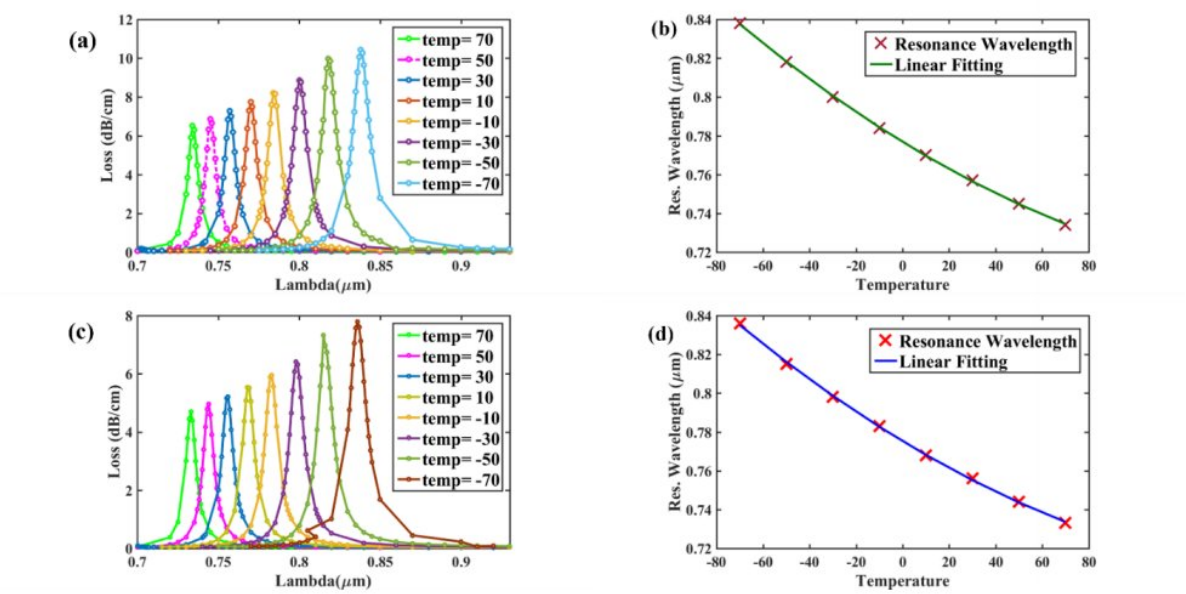

Fig. 6.12: [y-polarization] (a) CL curves for temp ranging from 70°C to -70°C; **(b)** curve fitting for loss curve in (a) for temperature variation; **[x-polarization] (c)** CL curves for temp ranging from 70°C to -70°C; **(d)** curve fitting for loss curve in (c) for temperature variation.

Fig. 6.12 (a), (c) shows as temperature decreases from 70°C to -70°C, RW shifts right and CL increases both for x-polarization and y-polarization which indicates that temperature can be easily detected with our sensor. Fig. 6.12 (b), (d) represents a 2nd order fitting between different temperatures and its resonance wavelengths respectively for x-polarization (R^2=0.9995) and y-polarization (R^2=0.9998).

The equation of the fitting curve for x-pol:

$$\lambda_{resonance} = 0.77522 - 0.0007244 \times T + 1.8601 \times 10^{-6} \times T^2 \quad (6.7)$$

and for y-pol:

$$\lambda_{resonance} = 0.77681 - 0.0007351 \times T + 1.875 \times 10^{-6} \times T^2 \quad (6.8)$$

here, T represents temperature and $\lambda_{resonance}$ represents resonance wavelength in μm for that temperature. The value of the resonant wavelength can be extracted from spectrum analyzer then substituting that value in either Equn. (6.7) or Equn. (6.8) depending on polarization, the temperature can be identified.

The maximum sensitivity we get is 1.05 nm/°C & 1 nm/°C and best resolution is 0.095°C & 0.1°C respectively for x-polarization and y-polarization. Sensitivity and other parameters at different temperatures is shown in Table 6.6 and 6.7 respectively for x-pol and y-pol. Table 6.8 shows the comparison between the performance of our proposed sensor and previously proposed sensors. It should be noted that our sensor's sensitivity can be increased a great amount only be replacing AZO by Au as plasmonic material. However, we have earlier chosen AZO to investigate our sensor performance because it provides sharp peak at resonance wavelength which is easy to detect.

Table 6.6

Performance analysis of proposed sensor as Temperature sensor (x-pol)

Temp (°C)	Resonant wavelength (μm)	Sensitivity (nm/°C)	Resolution
-70	0.836	1.05	0.09524
-50	0.815	0.85	0.11765
-30	0.798	0.75	0.133333
-10	0.783	0.75	0.133333
10	0.768	0.6	0.166667
30	0.756	0.6	0.166667
50	0.744	0.55	0.181818
70	0.733		

Table 6.7

Performance analysis of proposed sensor as Temperature sensor (y-pol)

Temp (°C)	Resonant wavelength (μm)	Sensitivity (nm/°C)	Resolution
-70	0.838	1	0.1
-50	0.818	0.9	0.111111111
-30	0.8	0.8	0.125
-10	0.784	0.7	0.142857143
10	0.77	0.65	0.153846154
30	0.757	0.6	0.166666667
50	0.745	0.55	0.181818182
70	0.734		

Table 6.8
Study of comparison with existing Temperature sensors

Reference	Sensitivity	Resolution	Sensing range
[94]	1.551	0.064	35°C to 100°C
[92]	0.75	0.133	-70°C to 70°C
[95]	0.229	0.437	25°C to 55°C
[96]	0.978	0.102	25°C to 100°C
[97]	1.25	0.08	-70°C to 70°C
[98]	4.67	0.03	30°C to 90°C
Our paper	1.05(x-pol)	0.09524	-70°C to 70°C
	1.00(y-pol)	0.1	

6.3.6 Double Step verification using Double peak shift sensitivity (DPSS)

It has been observed that our sensor exhibits three distinct loss peaks at three different resonance wavelength for refractive indices that are obtained during varying temperature from -70°C to 70°C. From Fig. 6.13 it is visible that as temperature increases the distance between two consecutive peaks decrease. Utilizing this phenomenon, we can calculate double peak shift sensitivity [99] for temperature in case of both 1st & 2nd peak and 2nd & 3rd peak which will able us to introduce a new method called 'Double step verification'. In this method we will first find out the double peak shift sensitivity (DPSS) for 1st and 2nd peak then for 2nd and 3rd peak, therefore by looking into both values we will determine the temperature. The equation used for DPSS is:

$$S_{DPSS}(T) = \frac{(\lambda_{p2} - \lambda_{p1})_{T_2} - (\lambda_{p2} - \lambda_{p1})_{T_1}}{T_2 - T_1} \times 10^3 (nm/°C) \quad (6.9)$$

where $S_{DPSS}(T)$ denotes double peak shift sensitivity of Temperature, λ_{p2,T_2} & λ_{p1,T_2} denotes RW for 2nd peak & 1st peak respectively for temperature T_2. Similarly, λ_{p2,T_1} & λ_{p1,T_1} denotes RW for 2nd peak & 1st peak respectively for temperature T_1.

The values of distance between two consecutive peaks (y-pol & x-pol) is shown in Fig 6.13 (a) & (b). The maximum DPSS is 0.35 nm/°C (both x-pol & y-pol) for 1st and 2nd peak and 1.9 nm/°C (x-pol) & .3 nm/°C (y-pol) for 2nd and 3rd peak. Detailed insights about distance difference is shown in Table 6.9.

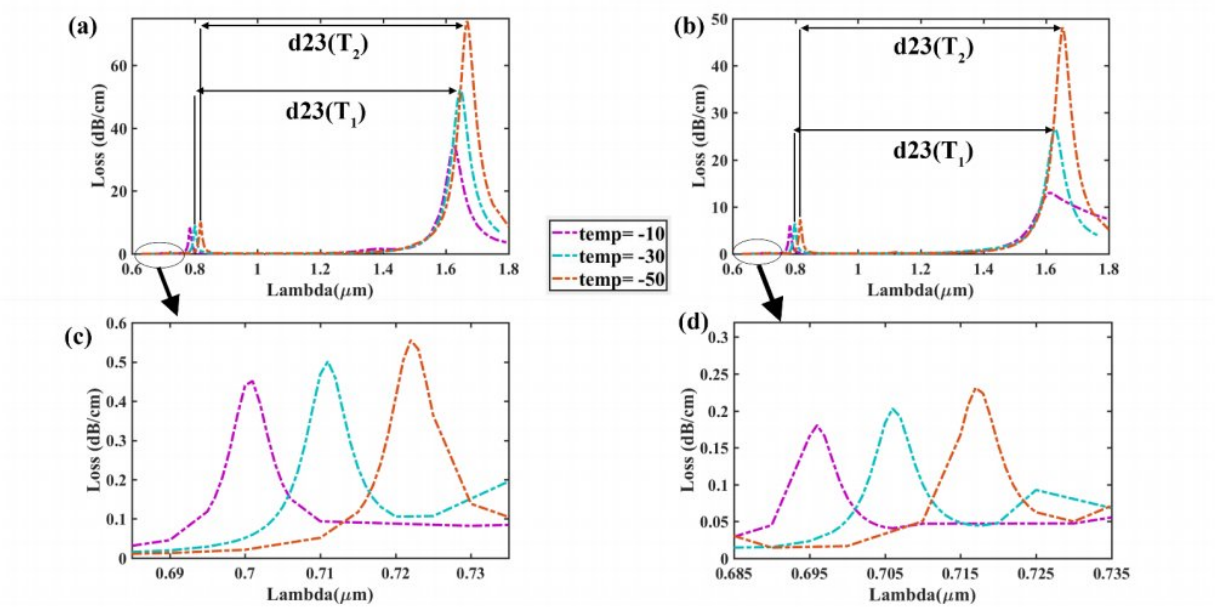

Fig. 6.13: [y-polarization] (a) Curves of 3 loss peaks due to temperature variation; (b) Curves of 3 loss peaks due to temperature variation; **[x-polarization]** (c) Zoomed portion of 1st loss peak; (d) Zoomed portion of 1st loss peak.

Along with the conventional method of identifying temperature where RW shift due to temperature variation is calculated, we have introduced a new method where the difference of distance between two consecutive peaks for temp. variation is calculated as shown in Fig. 6.13(a) and (b). Previously, M.R Islam et al. [99] introduced double peak shift sensitivity (DPSS) for RI detection, whereas our sensor use DPSS method for temperature detection and used our new proposed Double step verification.

Table 6.9
Analysis of Double Step Verification of Temperature Sensitivity

Temp (°C)	Polarization	d_{12}	d_{23}	S_{12}	S_{23}	Polarization	d_{12}	d_{23}	S_{12}	S_{23}
-50	x-pol	0.098	0.838	0.3	0.3	y-pol	0.096	0.849	0.35	0.2
-30		0.092	0.832	0.2	0.1		0.089	0.845	0.3	0.2
-10		0.088	0.83	0.35	1.9		0.083	0.841	0.2	0.3

6.4 Fabrication Tolerance Investigation & Future Fabrication Procedure

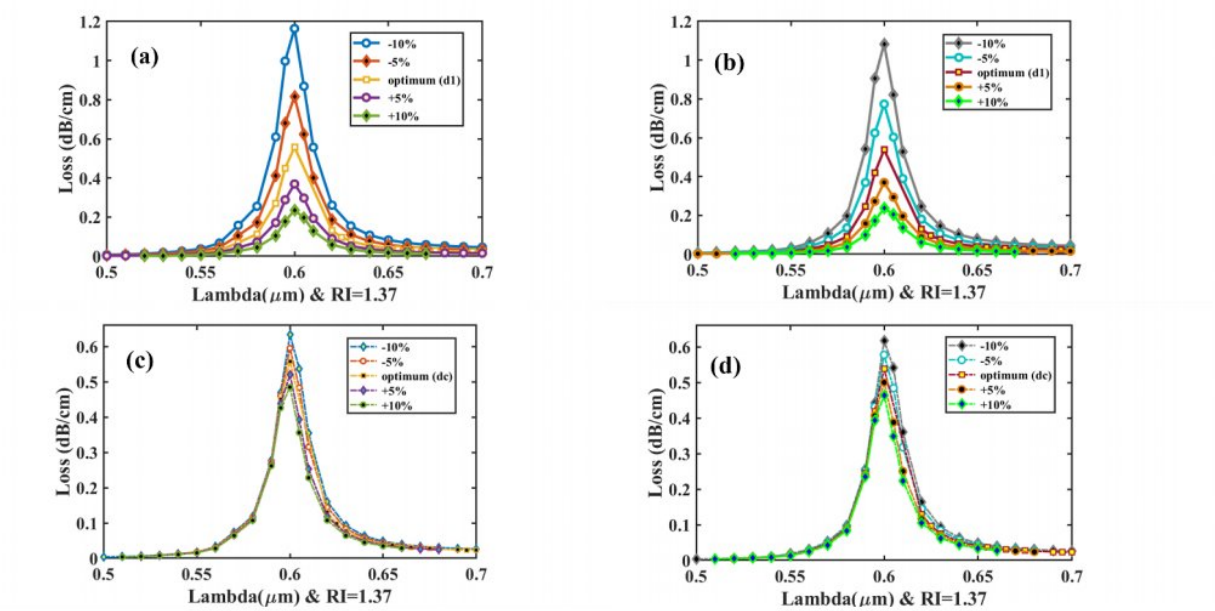

Fig. 6.14: Fabrication tolerance analysis- Effects of CL **[x-polarization] (a)** diameter -10%, -5%, +10% and +5% of d_1 ; **[y-polarization] (b)** diameter -10%, -5%, +10% and +5% of d_1 ; **[x-polarization]** (c) diameter -10%, -5%, +10% and +5% of d_c ; **[y-polarization] (d)** diameter -10%, -5%, +10% and +5% of d_c.

The suggested sensor's hexagonal structure may be effectively constructed using the well-known stack-and-draw fabrication technique [100]. Practically, fabricating the sensor with the precise design specifications is rather complicated. As a result, during manufacturing, deviations of up to ±1% or ±2% from the optimized values are considered thus it is necessary to check the fabrication tolerance (FT) analysis. Fig. 6.14 (a), (b), (c), and (d) demonstrated fluctuation in CL was extremely small and had no effect on sensor performance, and it is insignificant for diameter dimension d_1 & d_c changes of ±5% and ±10%.

6.5 Discussion

A multifunctional SPR-PCF sensor that is capable of RI sensing, temperature sensing as well as verifying it by double step verification is proposed in this chapter. Gold and AZO both used as the plasmonic material gives us different result and different sensing capabilities. Maximum AS for gold was found as 5269 RIU^{-1} and 5336 RIU^{-1} for x and y polarization respectively and WS was 36500 nm/RIU for x polarization and 40500nm/RIU for y polarization. AZO gave AS of 3593 RIU^{-1} and 3763 RIU^{-1} for x and y polarization respectively and WS of 8500 nm/RIU and 9100 nm/RIU for x and y respectively. The sensor gave a stunning RI detection range of 1.19 to 1.42 when AZO was used whereas it was only 1.32 to 1.43 for Gold. A sensor resolution, having Gold as the plasmonic material, of 46.4×10^{-6} RIU for x-pol and 46.3×10^{-6} RIU for y pol were found for Amplitude and 100×10^{-6} RIU was found for wavelength for both x and y-pol. Incorporating AZO, resulted in an AS of 16.1×10^{-6} RIU for x-pol and 15.5×10^{-6} for y-pol and WS of 200×10^{-6} was found for both x and y-pol. Temperature sensitivity obtained were 1.05 nm/^{o}C & 1 nm/^{o}C having a resolution of 0.095^{o}C and 0.1^{o}C respectively for x and y-pol. Furthermore, for double step verification that was proposed as a novel feature in this paper, maximum DPSS was 0.35 nm/^{o}C for 1st and 2nd peak and 1.9 nm/^{o}C (x-pol) & .3 nm/^{o}C (y-pol) for 2nd and 3rd peak. The tolerance exhibited by this sensor is exquisite which shows up to ±10% change in the geometric parameters so it can be easily realized using the Stack and Draw method. This sensor along with its different sensing abilities can be a major contributor to advancing analyte sensing using SPR and the double shift verification can be major breakthrough in opening a whole other world of temperature sensing.

Chapter 7
Concluding Remarks & Future Studies

7.1 Conclusion

We have studied all structural aspects in order to achieve the highest possible sensitivity and sensor resolution. As a general observation, the amplitude sensing method is avoided in practical implementations since it is regulated by the power fluctuations of the source and the detector, as well as optics. Many cross-sensitivity difficulties are eliminated in the case of WS. In the design of the set, we attempted to reduce loss and enhance sensitivity. We aimed to reduce propagation losses during core guided mode and plasma mode transmissions. One of the primary reasons for the originality of our structure is that it is produced using just circular air holes, making its fabrication simpler than other structures. Both of our concepts are suitable to manufacturing and have the potential to be applied in practice.

7.2 Socio-Economic Influence

Despite the fact that surface plasmon resonance (SPR) has been in use for around 20 years, a number of researchers continue to rely on antiquated techniques to determine biological interaction, despite the complexity and significance of SPR analysis. With the development of SPR-based research, SPR-based technology is becoming more affordable and accessible, allowing researchers to recognize the usefulness of SPR data. It is anticipated that SPR will become a standard method in all biochemistry laboratories since it reveals the true nature of entanglement. Surface plasmon resonance permits the identification of binding interactions between biomolecules. Evaluating the reciprocity between analytes and ligands without spending excessive time and money on expensive labeling reagents and processes is one of the most important characteristics of SPR-based technology. Experiments on binding kinetics need a minimum

number of specimens. The experiment's sensor chips are reusable, which reduces the total cost. Replication of experiments gives researchers with confidence in the correctness of the results. Widespread usage of SPR sensors has a significant influence on the detection of plasma, blood, and blood components in unidentified specimens in medical research. Monitoring of medicines, proteins, enzymes, and peptides using SPR sensing has made tremendous strides during the last several years. By detecting or analyzing the nucleic acids in bio fluids obtained from patients afflicted with Alzheimer's, diabetes, hepatitis leukemia, breast cancer, and prostate cancer, etc., SPR sensing has had a significant impact on medical conditions such as Alzheimer's, diabetes, hepatitis leukemia, breast cancer, and prostate cancer, among others. Due to the development of SPR-based sensors, food safety has witnessed significant gains. They are used to identify the quantity of alcohol in various alcoholic drinks, the concentration of E. coli, and the presence of polar compounds in oils. Pesticide, TNT, aromatic hydrocarbons, phenols, dioxins and residues, pathogens, microbial load, urea, phenolic components, hazardous proteins, and heavy metals are also discovered in food samples.

7.3 Future Studies

Although several PCF sensors have previously been modeled, not all the issues for such PCFs, such as the accurate light directing difficulty and the metal coating issue within air holes for internal sensing, have been resolved. Therefore, researchers continue to propose sensors to circumvent these obstacles. Titanium nitride (TiN)-based SPR sensors have lately acquired immense appeal due to the material's high melting point and chemical durability. We may use additional plasmonic materials, such as TiN and TiO to improve the results of this research. In the future, several forms of air holes that may provide superior outcomes will be examined. Using a bimetallic layer, we will also explore the change in the sensing characteristic.

References:

[1] M. R. Hasan *et al.*, "Spiral photonic crystal fiber-based dual-polarized surface plasmon resonance biosensor," *IEEE Sens. J.*, vol. 18, no. 1, pp. 133–140, 2018, doi: 10.1109/JSEN.2017.2769720.

[2] X. Yan, B. Li, T. Cheng, and S. Li, "Analysis of high sensitivity photonic crystal fiber sensor based on surface plasmon resonance of refractive indexes of liquids," *Sensors (Switzerland)*, vol. 18, no. 9, 2018, doi: 10.3390/s18092922.

[3] X. Chen, L. Xia, and C. Li, "Surface plasmon resonance sensor based on a novel D-shaped photonic crystal fiber for low refractive index detection," *IEEE Photonics J.*, vol. 10, no. 1, 2018, doi: 10.1109/JPHOT.2018.2790424.

[4] A. A. Rifat, M. R. Hasan, R. Ahmed, and H. Butt, "Photonic crystal fiber-based plasmonic biosensor with external sensing approach (erratum)," *J. Nanophotonics*, vol. 12, no. 01, p. 1, 2017, doi: 10.1117/1.jnp.12.019901.

[5] J. Ibrahim *et al.*, "Surface plasmon resonance based temperature sensors in liquid environment," *Sensors (Switzerland)*, vol. 19, no. 15, pp. 1–10, 2019, doi: 10.3390/s19153354.

[6] X. Zhou *et al.*, "High-Sensitivity SPR Temperature Sensor Based on Hollow-Core Fiber," *IEEE Trans. Instrum. Meas.*, vol. 69, no. 10, pp. 8494–8499, 2020, doi: 10.1109/TIM.2020.2992828.

[7] W. Yang *et al.*, "The Polydimethylsiloxane Coated Fiber Optic for All Fiber Temperature Sensing Based on the Multithin-Multifiber Structure," *IEEE Sens. J.*, vol. 21, no. 1, pp. 51–56, 2021, doi: 10.1109/JSEN.2020.2972292.

[8] Y. Wang, Q. Huang, W. Zhu, M. Yang, and E. Lewis, "Novel optical fiber SPR temperature sensor based on MMF-PCF-MMF structure and gold-PDMS film: erratum," *Opt. Express*, vol. 27, no. 8, p. 10813, 2019, doi: 10.1364/oe.27.010813.

[9] F. Wang, Z. Sun, T. Sun, C. Liu, P. K. Chu, and L. Bao, "Highly sensitive PCF-SPR biosensor for hyperthermia temperature monitoring," *J. Opt.*, vol. 47, no. 3, pp. 288–294, 2018, doi: 10.1007/s12596-018-0468-8.

[10] C. H. A. O. L. Iu *et al.*, "Symmetrical dual D-shape photonic crystal fibers for suIu, C. H. A. O. L., Eiquan, W. S. U., Iu, Q. I. L., Ili, X. L. U., Ang, F. A. W., Ao, T., Un, S., & Hu,

P. A. U. L. K. C. (2018). Symmetrical dual D-shape photonic crystal fibers for surface plasmon r," vol. 26, no. 7, pp. 481–490, 2018.

[11] P. K. Maharana, R. Jha, and S. Palei, "Sensitivity enhancement by air mediated graphene multilayer based surface plasmon resonance biosensor for near infrared," *Sensors Actuators B Chem.*, vol. 190, pp. 494–501, Jan. 2014, doi: 10.1016/J.SNB.2013.08.089.

[12] M. R. Hasan, S. Akter, K. Ahmed, and D. Abbott, "Plasmonic Refractive Index Sensor Employing Niobium Nanofilm on Photonic Crystal Fiber," *IEEE Photonics Technol. Lett.*, vol. 30, no. 4, pp. 315–318, 2018, doi: 10.1109/LPT.2017.2786475.

[13] G. An, S. Li, X. Yan, X. Zhang, Z. Yuan, and Y. Zhang, "High-sensitivity and tunable refractive index sensor based on dual-core photonic crystal fiber," *J. Opt. Soc. Am. B*, vol. 33, no. 7, p. 1330, 2016, doi: 10.1364/josab.33.001330.

[14] H. H. Qazi, A. B. Bin Mohammad, and M. Akram, "Recent progress in optical chemical sensors," *Sensors (Switzerland)*, vol. 12, no. 12, pp. 16522–16556, 2012, doi: 10.3390/s121216522.

[15] A. Upadhyay, S. Singh, Y. K. Prajapati, and R. Tripathi, "Numerical Analysis of Large Negative Dispersion and highly Birefringent Photonic Crystal Fiber," *Optik (Stuttg).*, vol. 218, no. May, p. 164997, 2020, doi: 10.1016/j.ijleo.2020.164997.

[16] L. G. Carrascosa, ``Molecular inversion probe-based SPR biosensing for specific, label-free and real-time detection of regional DNA methylation," *Chem. Commun.*, vol. 50, no. 27, pp. 3585_3588, 2014.

[17] E.K. Akowuah, T. Gorman, H. Ademgil, S. Haxha, G.K. Robinson, J.V. Oliver, Numerical analysis of a photonic crystal fiber for biosensing applications, IEEE J. Quantum Electron. 48 (11) (2012) 1403–1410.

[18] J.G. Ortega-Mendoza, A. Padilla-Vivanco, C. Toxqui-Quitl, P. Zaca-Morán, D. Villegas-Hernández, F. Chávez, Optical fiber sensor based on localized surface plasmon resonance using silver nanoparticles photodeposited on the optical fiber end, Sensors 14 (10) (2014) 18701–18710.

[19] B. Liedberg, C. Nylander, I. Lunström, Surface plasmon resonance for gas detection and biosensing, Sensors Actuators 4 (1983) 299–304.

[20] J. Homola, "Present and future of surface plasmon resonance biosensors," *Anal. Bioanal. Chem.*, 377, 528–539, 2003.

[21] R. Otupiri, E. Akowuah, S. Haxha, H. Ademgil, F. AbdelMalek, A. Aggoun, "A novel birefrigent photonic crystal fibre surface plasmon resonance biosensor," *IEEE Photon. J.*, 6, 2014.

[22] A.A. Rifat, R. Ahmed, A.K. Yestisen, H. Butt, A. Sabouri, G.A. Mahdiraji, S.H. Yun, F.r. Adikan, "Photonic crystal fiber based plasmonic sensors," *Sens. Actuatoros B Chem.* 243 (2017) 311–325.

[23] E. Kretschmann and H. Raether, "Notizen: Radiative Decay of Non Radiative Surface Plasmons Excited by Light", *Zeitschrift für Naturforschung A*, vol. 23, no. 12, 1968.

[24] B.D. Gupta, R.K. Verma, Surface plasmon resonance-based fiber optic sensors: principle, probe designs, and some applications, J. Sens. 2009 (2009) 979761.

[25] S. Chakma, M.A. Khalek, B.K. Paul, K. Ahmed, M.R. Hasan, A.N. Bahar, Gold-coated photonic crystal fiber biosensor based on surface plasmon resonance: design and analysis, Sens. Bio-Sens. Res. 18 (2018) 7–12.

[26] R.C. Jorgenson, S.S. Yee, A fiber-optic chemical sensor based on surface plasmon resonance, Sensors and Actuators B: Chemical, Volume 12, Issue 3, 1993, Pages 213-220.

[27] David Monzón-Hernández, Joel Villatoro, High-resolution refractive index sensing by means of a multiple-peak surface plasmon resonance optical fiber sensor, Sensors and Actuators B: Chemical, Volume 115, Issue 1, 2006, Pages 227-231.

[28] Suzuki, Hitoshi & Sugimoto, Mitsunori & Matsui, Yoshikazu & Kondoh, Jun. (2006). Fundamental characteristics of a dual-colour fibre optic SPR sensor. Measurement Science and Technology. 17. 1547. 10.1088/0957-0233/17/6/036.

[29] R. Ritchie, Plasma losses by fast electrons in thin films, Phys. Rev. 106 (1957) 874.

[30] W. Qin, S. Li, Y. Yao, X. Xin, J. Xue, Analyte-filled core self-calibration microstructured optical fiber based plasmonic sensor for detecting high refractive index aqueous analyte, Opt. Lasers Eng. 58 (2014) 1–8.

[31] J. N. Dash and R. Jha, "Graphene-based birefringent photonic crystal fiber sensor using surface plasmon resonance," IEEE Photonics Technology Letters 26, 1092- 1095 (2014)

[32] J.N Dash and Rajan Jha, "Surface plasmon resonance biosensor based on polymer photonic crystal fibers coated with conducting metal oxide", *IEEE Photonics Technology Letter,* vol. 26, no. 6, pp. 595-598, March 2014.

[33] C. Caucheteur, T. Guo, and J. Albert, "Review of plasmonic fiber optic biochemical sensors: improving the limit of detection," Analytical and bioanalytical chemistry 407, 3883-3897 (2015).

[34] Q. Liu, S. Li, H. Chen, J. Li, and Z. Fan, "High-sensitivity plasmonic temperature sensor based on photonic crystal fiber coated with nanoscale gold film," Applied Physics Express 8, 046701 (2015).

[35] N. Luan, R. Wang, W. Lv, and J. Yao, ``Surface plasmon resonance sensor based on D-shaped microstructured optical fiber with hollow core," *Opt. Express*, vol. 23, no. 7, pp. 8576_8582, Mar. 2015.

[36] A. A. Rifat, R. Ahmed, G. A. Mahdiraji, and F. M. Adikan, ``Highly sensitive D-shaped photonic crystal fiber-based plasmonic biosensor in visible to near-IR," IEEE Sensors J., vol. 17, no. 9, pp. 2776_2783, Jun. 2017.

[37] R. K. Gangwar and V. K. Singh, "Highly sensitive surface plasmon resonance based D-shaped photonic crystal fiber refractive index sensor," Plasmonics 1–6 (2016).

[38] Q. Xie et al., "Characteristics of D-shaped photonic crystal fiber surface plasmon resonance sensors with different side-polished lengths," Appl. Opt. 56(5), 1550–1555 (2017).

[39] M. Tian et al., "All-solid D-shaped photonic fiber sensor based on surface plasmon resonance," Opt. Commun. 285(6), 1550–1554 (2012).

[40] W. Qin, S. Li, Y. Yao, X. Xin, and J. Xue, "Analyte-filled core self-calibration microstructured optical fiber based plasmonic sensor for detecting high refractive index aqueous analyte," *Opt. Lasers Eng.*, vol. 58, pp. 1–8, 2014, doi: 10.1016/j.optlaseng.2014.01.003.

[41] R. K. Gangwar and V. K. Singh, "Highly Sensitive Surface Plasmon Resonance Based D-Shaped Photonic Crystal Fiber Refractive Index Sensor," *Plasmonics*, vol. 12, no. 5, pp. 1367–1372, 2017, doi: 10.1007/s11468-016-0395-y.

[42] I. Danlard and E. K. Akowuah, "Design and Theoretical Analysis of a Dual-Polarized Quasi D-Shaped Plasmonic PCF Microsensor for Back-to-Back Measurement of Refractive Index and Temperature," *IEEE Sens. J.*, vol. 21, no. 8, pp. 9860–9868, 2021, doi: 10.1109/JSEN.2021.3058224.

[43] A. K. Shakya, A. Ramola, S. Singh, and V. Van, "Design of an ultra-sensitive bimetallic anisotropic PCF SPR biosensor for liquid analytes sensing," *Opt. Express*, vol. 30, no. 6, p. 9233, 2022, doi: 10.1364/oe.432263.

[44] M. R. Islam *et al.*, "Design of a Dual Cluster and Dual Array-Based PCF-SPR Biosensor with Ultra-high WS and FOM," *Plasmonics*, no. Cl, 2022, doi: 10.1007/s11468-022-01612-z.

[45] J.-K. Wang, Y. Ying, Z.-J. Gao, S.-Y. Cheng, and G.-Y. Si, "Surface plasmon resonance (SPR) based temperature and magnetic field sensor in a dual-core D-shaped photonic crystal fiber (PCF)," *Instrum. Sci. Technol.*, vol. 50, no. 3, pp. 271–287, 2022, doi: 10.1080/10739149.2021.1994417.

[46] J. A. Buck, "Fundamentals of Optical Fibers," John Wiley and Sons Inc., USA, 2ndEdition, 2004.

[47] K. Kaneshima, Y. Namihira, N. Zou, H. Higa, and Y. Nagata, "Numerical investigation of octagonal photonic crystal fibers with strong confinement field," IEICE Transactions on Electronics, vol. E89-C, no. 6, pp. 830-837, 2006

[48] D. Ferrarini, L. Vincetti, M. Zoboli, A. Cucinotta, and S. Selleri, "Leakage properties of photonic crystal fibers," Optics Express, vol. 10, no. 23, pp.1314-1319, 2002.

[49] G. P. Agrawal, "Nonlinear Fiber Optics," Academic Press, 2nd Edition, 1995.

[50] X. Yang, et al., Analysis of graphene-based photonic crystal fiber sensor using Birefringence and surface plasmon resonance, Plasmonics 12 (2) (2017) 489–496

[51] C. Mouvet, R. Harris, C. Maciag, B. Luff, J. Wilkinson, J. Piehler, et al., Determination of simazine in water samples by waveguide surface plasmon resonance, Anl. Chim. Acta 338 (1997) 109–117.

[52] S. Chowdhury, S. Sen, K. Ahmed, B.K. Paul, M.B.A. Miah, S. Asaduzzaman, M.S. Islam, M.I. Islam, Porous shaped photonic crystal fiber with strong confinement field in sensing applications: design and analysis, Sens. Bio-Sens. Res. 13 (1) (2017) 63–69.

[53] Md. Selim Habib, Md. Samiul Habib, S.M. Abdur Razzak, Yoshinori Namihira, M.A. Hossain, and M.A. Goffar Khan, "Broadband dispersion compensation of conventional single mode fibers using microstructure optical fibers," Optik, vol. 124, no. 19, pp. 3851-3855, Oct. 2013.

[54] E.K. Akowuah, T. Gorman, H. Ademgil, S. Haxha, G.K. Robinson, J.V. Oliver, Numerical analysis of a photonic crystal fiber for biosensing applications, IEEE J. 51 Quantum Electron. 48 (2012) 1403–1410

[55] Y . Lu, et al., SPR sensor based on polymer photonic crystal fibers with metal nanolayers, Sensors 13 (Jan. 2013) 956–965

[56] E.K. Akowuah, et al., A highly sensitive photonic crystal fibre (PCF)surface plasmon resonance (SPR) sensor based on a bimetallic structureof gold and silver, Proc. IEEE 4th Int. Conf. on Adaptive Scienceand Technology, 2012, pp. 121–125

[57] Z. Tan, et al., Improving the sensitivity of fiber surface plasmon resonance sensor by filling liquid in a hollow core photonic crystal fiber, Plasmonics 9 (1) (2014) 167–173

[58] Md. Selim Habib, Md. Samiul Habib, and S.M.A. Razzak, "Study on dual-concentric-core dispersion compensating photonic crystal fiber," International J. of Eng. and Technol., vol. 1, no. 4, pp. 377-383, 2012

[59] Hikmat N. Daghestani1 and Billy W. Day2*, "Theory and Applications of Surface Plasmon Resonance, Resonant Mirror, Resonant Waveguide Grating, and Dual Polarization Interferometry Biosensors," Sensors, vol. 10, pp. 9630-9646, Nov. 2010.

[60] Bertrand Gauvreau, Alireza Hassani, Majid Fassi Fehri, Andrei Kabashin, Maksim Skorobogatiy, "Photonic bandgap fiber-based Surface Plasmon Resonance sensors," Optic Express, vol. 15, no. 18, pp. 11413-11426, Sep. 2007.

[61] Descrovi, E., Paeder, V., Vaccaro, L., & Herzig, H.-P. A virtual optical probe based on localized Surface Plasmon Polaritons. Optics Express, 13(18), 7017. doi:10.1364/opex.13.007017, 2005

[62] Md. Selim Habib, Md. Samiul Habib, S.M. Abdur Razzak, Yoshinori Namihira, M.A. Hossain, and M.A. Goffar Khan, "Broadband dispersion compensation of conventional single mode fibers using microstructure optical fibers," Optik, vol. 124, no. 19, pp. 3851-3855, Oct. 2013.

[63] Islam, M.R., Iftekher, A.N.M., Hasan, K.R. et al. Surface plasmon resonance based highly sensitive gold coated PCF biosensor. Appl. Phys. A 127, 118 (2021). https://doi.org/10.1007/s00339-020-04162-5.

[64] Mohammad Rakibul Islam, Md. Abu Jamil, Md. Siraz-Uz Zaman, Syed Asir Hamim Ahsan, Mahfuz Kabir Pulak, Fariha Mehjabin, Md Moinul Islam Khan, Jubair Alam Chowdhury, Mohibul Islam, Design and analysis of birefringent SPR based PCF biosensor with ultra-high sensitivity and low loss, Optik, Volume 221, 2020

[65] M. S. Islam et al., "A Hi-Bi Ultra-Sensitive Surface Plasmon Resonance Fiber Sensor," in IEEE Access, vol. 7, pp.79085-79094, 2019, doi: 10.1109/ACCESS.2019.2922663.

[66] Md. Saiful Islam, Mohammad Rakibul Islam, Jakeya Sultana, Alex Dinovitser, Brian W.-H. Ng, and Derek Abbott, "Exposed-core localized surface plasmon resonance biosensor," J. Opt. Soc. Am. B **36**, 2306-2311 (2019)

[67] D. Li, W. Zhang, H. Liu, J. Hu, and G. Zhou, "High sensitivity refractive index sensor based on multicoating photonic crystal fiber with surface plasmon resonance at near-infrared wavelength," IEEE Photonics Journal, vol. 9, no. 2, pp. 1-8, 2017.

[68] M. A. Mollah, A. K. Paul, and S. M. A. Razzak, "Dual Polarized Plasmonic Refractive Index Sensor based on Photonic Crystal Fiber," International Conference on Electrical and Computer Engineering., 2018.

[69] Md. Saiful Islam, Jakeya Sultana, Rifat Ahmmed Aoni, Md. Selim Habib, Alex Dinovitser, Brian W.-H. Ng, and Derek Abbott, "Localized surface plasmon resonance biosensor: an improved technique for SERS response intensification," Opt. Lett. 44, 1134-1137 (2019)

[70] Md. Nazmul Hossen, Md. Ferdous, Md. Abdul Khalek, Sujan Chakma, Bikash Kumar Paul, Kawsar Ahmed, "Design and analysis of biosensor based on surface plasmon resonance," Sensing and Bio-sensing Research, vol. 21, pp. 1-6, 2018

[71] Md. Saiful Islam, Jakeya Sultana, Ahmmed. A. Rifat, Rajib Ahmed, Alex Dinovitser, Brian W.-H. Ng, Heike Ebendorff-Heidepriem, and Derek Abbott, "Dual-polarized highly sensitive plasmonic sensor in the visible to near-IR spectrum," Opt. Express 26, 30347-30361 (2018)

[72] Ahmmed A. Rifat, Firoz Haider, Rajib Ahmed, Ghafour Amouzad Mahdiraji, F. R. Mahamd Adikan, and Andrey E. Miroshnichenko, "Highly sensitive selectively coated photonic crystal fiber-based plasmonic sensor," Opt. Lett. 43, 891-894 (2018)

[73] Sujan Chakma, Md Abdul Khalek, Bikash Kumar Paul, Kawsar Ahmed, Md Rabiul Hasan, Ali Newaz Bahar,Gold-coated photonic crystal fiber biosensor based on surface plasmon resonance: Design and analysis,Sensing and Bio-Sensing Research,Volume 18,2018,Pages 7-12,ISSN 2214-1804

[74] F. Haider, R. A. Aoni, R. Ahmed, M. S. Islam, and A. E. Miroshnichenko, "Propagation Controlled Photonic Crystal Fiber-Based Plasmonic Sensor via Scaled-Down Approach," *IEEE Sens. J.*, vol. 19, no. 3, pp. 962–969, 2019, doi: 10.1109/JSEN.2018.2880161.

[75] V. Kaur and S. Singh, "Design of titanium nitride coated PCF-SPR sensor for liquid sensing applications," *Opt. Fiber Technol.*, vol. 48, no. March, pp. 159–164, 2019, doi: 10.1016/j.yofte.2018.12.015.

[76] Islam, Mohammad Rakibul *et al.*, "Highly birefringent gold-coated SPR sensor with extremely enhanced amplitude and wavelength sensitivity," *Eur. Phys. J. Plus*, vol. 136, no. 2, p. 238, 2021, doi: 10.1140/epjp/s13360-021-01220-6.

[77] M. R. Islam *et al.*, "An Eye-Shaped Ultra-Sensitive Localized Surface Plasmon Resonance–Based Biochemical Sensor," *Plasmonics*, vol. 17, no. 1, pp. 131–141, 2022, doi: 10.1007/s11468-021-01501-x.

[78] M. S. Islam *et al.*, "Dual-polarized highly sensitive plasmonic sensor in the visible to near-IR spectrum," *Opt. Express*, vol. 26, no. 23, p. 30347, 2018, doi: 10.1364/oe.26.030347.

[79] M. Al Mahfuz, M. R. Hasan, M. R. Momota, A. Masud, and S. Akter, "Asymmetrical photonic crystal fiber based plasmonic sensor using the lower birefringence peak method," *OSA Contin.*, vol. 2, no. 5, p. 1713, 2019, doi: 10.1364/osac.2.001713.

[80] M. Al Mahfuz *et al.*, "Highly sensitive photonic crystal fiber plasmonic biosensor: Design and analysis," *Opt. Mater. (Amst).*, vol. 90, pp. 315–321, 2019, doi: 10.1016/j.optmat.2019.02.012.

[81] M. R. Islam *et al.*, "Design and analysis of birefringent SPR based PCF biosensor with ultra-high sensitivity and low loss," *Optik (Stuttg).*, vol. 221, no. May, p. 165311, 2020, doi: 10.1016/j.ijleo.2020.165311.

[82] M. S. Islam, M. R. Islam, J. Sultana, A. Dinovitser, B. W.-H. Ng, and D. Abbott, "Exposed-core localized surface plasmon resonance biosensor," *J. Opt. Soc. Am. B*, vol. 36, no. 8, p. 2306, 2019, doi: 10.1364/josab.36.002306.

[83] E. Haque, M. A. Hossain, F. Ahmed, and Y. Namihira, "Surface Plasmon Resonance Sensor Based on Modified D-Shaped Photonic Crystal Fiber for Wider Range of Refractive Index Detection," *IEEE Sens. J.*, vol. 18, no. 20, pp. 8287–8293, 2018, doi: 10.1109/JSEN.2018.2865514.

[84] F. Haider, R. A. Aoni, R. Ahmed, and A. E. Miroshnichenko, "Highly amplitude-sensitive photonic-crystal-fiber-based plasmonic sensor," *J. Opt. Soc. Am. B*, vol. 35, no. 11, p. 2816, 2018, doi: 10.1364/josab.35.002816.

[85] H. Thenmozhi, M. S. Mani Rajan, and K. Ahmed, "D-shaped PCF sensor based on SPR for the detection of carcinogenic agents in food and cosmetics," *Optik (Stuttg).*, vol. 180, pp. 264–270, 2019, doi: 10.1016/j.ijleo.2018.11.098.

[86] M. R. Islam *et al.*, "Design and Analysis of a Biochemical Sensor Based on Surface Plasmon Resonance with Ultra-high Sensitivity," *Plasmonics*, vol. 16, no. 3, pp. 849–861, 2021, doi: 10.1007/s11468-020-01355-9.

[87] M. R. Islam *et al.*, "Surface plasmon resonance based highly sensitive gold coated PCF biosensor," *Appl. Phys. A Mater. Sci. Process.*, vol. 127, no. 2, 2021, doi: 10.1007/s00339-020-04162-5.

[88] D. Li, W. Zhang, H. Liu, J. Hu, and G. Zhou, "High Sensitivity Refractive Index Sensor Based on Multicoating Photonic Crystal Fiber with Surface Plasmon Resonance at Near-Infrared Wavelength," *IEEE Photonics J.*, vol. 9, no. 2, 2017, doi: 10.1109/JPHOT.2017.2687121.

[89] M. R. Hasan *et al.*, "Spiral photonic crystal fiber-based dual-polarized surface plasmon resonance biosensor," *IEEE Sens. J.*, vol. 18, no. 1, pp. 133–140, 2018, doi: 10.1109/JSEN.2017.2769720.

[90] M. R. Momota and M. R. Hasan, "Hollow-core silver coated photonic crystal fiber plasmonic sensor," *Opt. Mater. (Amst).*, vol. 76, pp. 287–294, 2018, doi: 10.1016/j.optmat.2017.12.049.

[91] Y. Yu *et al.*, "Some features of the photonic crystal fiber temperature sensor with liquid ethanol filling," *Opt. Express*, vol. 18, no. 15, p. 15383, 2010, doi: 10.1364/oe.18.015383.

[92] M. Rakibul Islam, M. M. I. Khan, F. Mehjabin, J. Alam Chowdhury, and M. Islam, "Design of a fabrication friendly & highly sensitive surface plasmon resonance-based photonic crystal fiber biosensor," *Results Phys.*, vol. 19, no. August, p. 103501, 2020, doi: 10.1016/j.rinp.2020.103501.

[93] M. Abbasi, M. Soroosh, and E. Namjoo, "Polarization-insensitive temperature sensor based on liquid filled photonic crystal fiber," *Optik (Stuttg).*, vol. 168, pp. 342–347, 2018, doi: 10.1016/j.ijleo.2018.04.116.

[94] Y. Wang, Q. Huang, W. Zhu, M. Yang, and E. Lewis, "Novel optical fiber SPR temperature sensor based on MMF-PCF-MMF structure and gold-PDMS film: erratum," *Opt. Express*, vol. 27, no. 8, p. 10813, 2019, doi: 10.1364/oe.27.010813.

[95] X. Mo, J. Lv, Q. Liu, X. Jiang, and G. Si, "A magnetic field SPR sensor based on temperature self-reference," *Sensors*, vol. 21, no. 18, pp. 1–9, 2021, doi: 10.3390/s21186130.

[96] S. Liu, S. Cao, Z. Zhang, Y. Wang, C. Liao, and Y. Wang, "Temperature sensor based on side-polished fiber SPR device coated with polymer," *Sensors (Switzerland)*, vol. 19, no. 19, 2019, doi: 10.3390/s19194063.

[97] M. R. Islam *et al.*, "Trigonal cluster-based ultra-sensitive surface plasmon resonance sensor for multipurpose sensing," *Sens. Bio-Sensing Res.*, vol. 35, no. January, p. 100477, 2022, doi: 10.1016/j.sbsr.2022.100477.

[98] M. K. Hasan, M. M. Rahman, M. S. Anower, M. M. Rana, A. K. Paul, and K. Chakrabatri, "Design and Analysis of Plasmonic Temperature Sensor Utilizing Photonic Crystal Fiber," *2020 IEEE Reg. 10 Symp. TENSYMP 2020*, no. July, pp. 1189–1192, 2020, doi: 10.1109/TENSYMP50017.2020.9230804.

[99] M. Rakibul Islam, A. N. M. Iftekher, M. S. Anzum, M. Rahman, and S. Siraz, "LSPR Based Double Peak Double Plasmonic Layered Bent Core PCF-SPR Sensor for Ultra-Broadband Dual Peak Sensing," *IEEE Sens. J.*, vol. 22, no. 6, pp. 5628–5635, 2022, doi: 10.1109/JSEN.2022.3149715.

[100] M. F. Azman, G. A. Mahdiraji, W. R. Wong, R. A. Aoni, and F. R. M. Adikan, "Design and fabrication of copper-filled photonic crystal fiber based polarization filters," *Appl. Opt.*, vol. 58, no. 8, pp. 2068–2075, Mar. 2019, doi: 10.1364/AO.58.002068.